Review

Advancements and Perspectives in Additive Manufacturing of Tungsten Alloys and Composites: Challenges and Solutions

Mehrdad Zarinejad *, Yunxiang Tong *, Mojtaba Salehi *, Chengfa Mu, Nian Wang, Yonglong Xu, Sajjad Rimaz, Lintao Tian, Kai Xiang Kuah, Xiaotong Chen

Posted Date: 17 June 2024

doi: 10.20944/preprints202406.1108.v1

Keywords: Refractory materials; laser powder bed fusion; directed energy deposition; electron beam melting

Review

Advancements and Perspectives in Additive Manufacturing of Tungsten Alloys and Composites: Challenges and Solutions

Mehrdad Zarinejad [1,2,*], Yunxiang Tong [3,*], Mojtaba Salehi [4,*], Chengfa Mu [1], Nian Wang [2], Yonglong Xu [2], Sajjad Rimaz [5], Lintao Tian [1], Kai Xiang Kuah [6] and Xiaotong Chen [1]

[1] Research and Development Institute, Wenzhou Hongfeng Electrical Alloy Co. Ltd., No.5600, Oujin Avenue, Oujiangkou Industry Cluster, Wenzhou, Zhejiang, China
[2] Wenzhou Hongfeng Alloy Co. Ltd., No.1633 Binhai First Avenue, Wenzhou Economic and Technology Development Zone, Wenzhou, Zhejiang, China
[3] Institute of Materials Processing and Intelligent Manufacturing, College of Materials Science and Chemical Engineering, Harbin Engineering University, Harbin, 150001, China
[4] Additive Manufacturing Division, Singapore Institute of Manufacturing Technology (SIMTech), Agency for Science, Technology and Research (A*STAR), 5 Cleantech Loop, 636732, Singapore
[5] Department of Chemical and Bimolecular Engineering, National University of Singapore, 4 Engineering Drive 4, 117585, Singapore
[6] Department of Materials Science and Engineering, National University of Singapore, 9 Engineering Drive 1, 117575, Singapore
* Correspondence: mehrdad@wzhf.com; ongyx@hrbeu.edu.cn; Mojtaba_salehi@simtech.a-star.edu.sg

Abstract: This review examines additive manufacturing for refractory tungsten (W) and its alloys. It emphasizes the primary challenges and determining factors involved in additive manufacturing pure W, W alloys, and composites. Our focus in this regard extends to both process and alloying strategies designed to address critical issues such as densification, micro-cracking, and mechanical properties in tungsten-based components produced through additive techniques. Throughout the review, we organize existing knowledge and insights into convenient tables, serving as valuable resources for researchers embarking on a deeper exploration of these topics.

Keywords: refractory materials; laser powder bed fusion; directed energy deposition; electron beam melting

1. Introduction

Additive manufacturing (AM) of refractory alloys offers unparalleled design freedom, optimizing both lightweight and durable structures crucial for aerospace and automotive sectors. Unlike traditional subtractive techniques that can waste up to 70% of material [1–3], AM's layer-by-layer approach ensures material efficiency, especially with costly refractory alloys [4,5]. The domain of rapid prototyping, customization, repair, and remanufacturing has been significantly enhanced with AM, accelerating prototype testing, and introducing new possibilities for alloys and healthcare implants [6,7]. Through controlled microstructures, AM has given rise to innovative materials and composites with improved properties, from titanium (Ti) alloys with increased strength [8,9] to functionally graded materials (FGMs) [10,11] and metal matrix composites (MMCs) [12–15]. Innovations are further propelled by integrating AI and machine learning, optimizing refractory alloy AM processes [16–20]. Broader implications of AM use encompass environmental, socio-economic, and regulatory aspects [21–24]. AM not only champions resource efficiency but also aligns with the circular economy's principles, promising reduced environmental footprints and reshaping the labor market. However, with AM's growing prominence in different sectors, evolving regulatory frameworks to ensure output quality is paramount.

 doi:10.20944/preprints202406.1108.v1

Refractory alloys, including tungsten (W) and its alloys, are integral to aerospace, automotive, and energy generation industries [25]. Tungsten is well known for its high melting point (approximately 3370°C), good mechanical properties, and low thermal expansion coefficient of less than 4 μm/m·K [26]. Additionally, its impressive thermal conductivity, surpassing 150 W/m·K [26], exceptional resistance to heat and wear [27], notable chemical stability, and remarkable hardness [27] make it suitable for high-temperature and radiation-resilient applications. Examples of its applications include collimators, heat sinks [28], integrated circuits [29,30], switch contacts [31], rocket nozzles [29,32], turbine blades [29], and nuclear reactor parts [29,33]. However, harnessing the full potential of refractory alloys, particularly those of W, has been challenging owing to their complex metallurgical behavior and high melting points [34]. These challenges include economic constraints [35], scalability issues, and difficulties in creating intricate structures, which have historically impeded the fabrication of refractory alloys [35].

Although the AM of W parts can mitigate many of the issues stated above, other significant challenges need to be overcome. The high melting points and elevated ductile-to-brittle transition temperatures (DBTT) pose concerns for all refractory alloys but are amplified for W because of its high viscosity (8 × 10−3 Pa·s) [36], surface tension (2.361 N/m) [36], and rapid solidification rate [37]. In the solid state, W's body-centered cubic (BCC) structure adds complexity to thermal processes, particularly given its DBTT [38,39] and the notable influence of impurities on its DBTT. Issues such as interstitial contamination, balling [40], limited understanding of process-structure-property relationships [37,40], cracking [41], and challenges in joining AM-fabricated W parts [42] represent substantial hurdles to overcome. Nevertheless, the potential of AM in refractory alloys and W broadens the spectrum of multidimensional opportunities, extending beyond traditional technological applications [43].

Over the past decade, extensive research has been undertaken on the AM of unalloyed and alloyed W, as well as W-matrix composites [43,44]. Most studies on unalloyed W have utilized laser powder bed fusion through selective laser melting (LPBF-SLM) [32,36–38,40,43,45–80], and electron beam melting (EBM) [52,53,66,78–88] of W. Other notable methods employed include laser-direct energy deposition (L-DED) [26,53,66,78–80,89], wire arc additive manufacturing (WAAM) [90], the emerging laser melting deposition [91–97], and the binder jetting additive manufacturing (BJAM), which shows immense promise for W-based materials [98–102]. Other novel methods such as ultrashort-time liquid phase sintering (LPS) [103], and bound metal deposition (BMD) have also been introduced [104]. Research on AM of W alloys and composites using the same techniques, which will be referred to and discussed in subsequent sections, is also evolving rapidly. These studies collectively underscore that the AM of W materials necessitates an intricate understanding of materials science in liquid and solid states and thermodynamics. In most AM processes, W material initially melts, and then solidifies, leading to nucleation and subsequent grain growth. This thermal history contrasts with traditional processing techniques like sintering, which primarily deals with powder densification followed by grain growth. Post-solidification grain growth in AM shares similarities with sintering, and is guided by kinetic laws [79,105]. However, in AM of nano-W, surface diffusion prevails [79,106], unlike traditional sintering's grain boundary diffusion. Recognizing these differences and understanding the influence of process parameters and alloy chemistry on molten pool behavior, solidification, and further solid-state microstructural evolution and strengthening effects are crucial [43,79,94,107–109].

This study comprehensively reviews AM techniques for W-based materials. We start by providing the current status of the techniques for the AM of W and its alloys, including selective laser melting (SLM), directed energy deposition (DED), and electron beam melting (EBM). We will then look at the challenges that are often associated with their AM processes, such as densification, microcracking, and limited material properties, followed by mitigation strategies that researchers have developed from the design and material perspectives to address the above concerns. Finally, our review concludes with promising future directions for the AM of W, aimed at paving the way for their broader adoption and commercialization.

 doi:10.20944/preprints202406.1108.v1

2. Techniques for Additive Manufacturing of Tungsten and Tungsten Alloys

The fabrication of W and W-based metal systems requires significant energy input. For instance, an energy input of more than 400 J/mm^3 may not suffice for the direct melting of W [32,79,110]. Due to technological advancements, AM systems have been equipped with high-energy sources like lasers and electrons to provide the energy required. A brief account of AM methods, outlining their application in W fabrication and highlighting their operational differences is presented below.

Table 1 provides a brief comparison of process parameters and relative densities of W achieved via different techniques for AM of W-based refractory materials (element, alloys, and composites), including LPBF-SLM, L-DED, EBM, as well as the emerging technologies, LMD and BJAM. Figure 1 depicts the schematic setups of these methods [111–115].

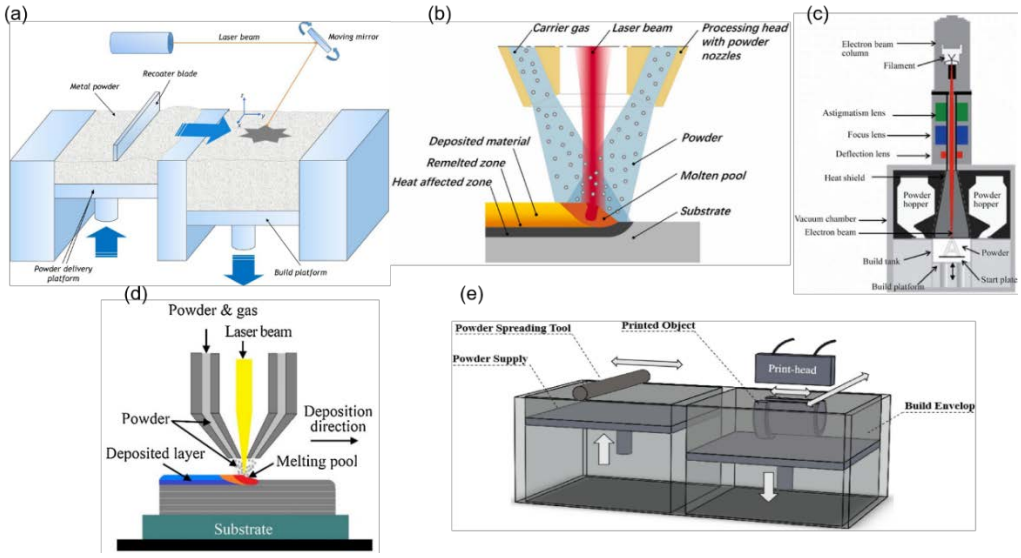

Figure 1. Schematic set-ups of AM techniques used for W materials: a) LPBF-SLM [111], b) L-DED [112], c) EBM [113], d) LMD [114], e) BJAM [115].

Table 1. A brief comparison of LPBF, Laser DED, EBM LMD and BJAM techniques for AM of W materials.

AM Process	Energy (W)	Beam Size (µm)	Scan Speed (mm/s)	Temperature Gradient (°C/mm)	Cooling Rate (°C/s)	Relative Density (%)	Remark
LPBF-SLM	10^2-10^3 (normally below 1000 [79,80,116])	30-200 [80,116]	10-10^3 [116]	10^6-10^7 [80,116] ;	10^5-10^7 [80,116]	95 [66,73] and max. ~98.71 [49]	A general processing window exists for SLM-fabrication of W (Figure 4b [36]). Laser techniques, like femtosecond fiber laser, are advantageous for AM of W [37]. The double melt strategy improves W densification in LPBF [65]. SLM can be merged with other processes, e.g., infiltration, for W-based materials [38].

 doi:10.20944/preprints202406.1108.v1

L-DED	10^2-10^4 [91,116] (normally between 600-4000 [80])	10^2 -10^3 [80,116]	10-10^2 [80,116]	10^4-10^6 [80,91,116]	10^2-10^5 [116], mostly on the order of 10^4 °C/s [38]	More than 99 for W [26]: even higher for W alloys [50]	In L-DED, the relationship between molten pool size and powder flow is crucial (Figure 5b, d) [28]. Increased laser energy widens the molten pool, but if the molten pool exceeds the flow of the powder, it can result in the reduction in the percentage of W entering [26]. L-DED surpasses EBM and LPBF in fabricating larger parts [26].
EBM	10^2-10^3 [80,116] (Normally more than 1000 W up to 3000 W [51,79,82] but can be as high as 6000	10^2 -10^3 [80,116]	10-10^3 [116]		10^3-10^4 [80,91,116]	~99.5 in W [51]	EBM requires a high vacuum level post He/N_2 purge due to electron travel [51,82]. The EBM processing window is depicted using scanning speed and current (or current density) in Figure 4a [51,79]. EBM, with appropriate preheating, can address cracking issues in AM for W materials [51,80,81]. EBM-fabricated W show promising results [51,79,81]. EBM has been adapted for W surface treatment to enhance quality, due to its controlled beam size and thermal influence on parts [88].
LMD (Laser melting Deposition)	10^2-10^3 [91,96]	10^3 [91,96]	10-10^3 [96]	less than L-PBF-SLM	10^3-10^4 [80,96]	99 [91] to Nearly 100 [97] for WHA	LMD provides comparatively large melt pools (on the order of several millimeters) versus SLM (on the order of 100 μm). [91,96] LMD's larger melt pools and slower cooling rates [96,116] aid in W particle organization and

 doi:10.20944/preprints202406.1108.v1

			decrease porosity [92–95]
BJ (Binder Jetting)		99.7 for WHA [98]	Uses a flowable powder and polymer adhesive on a build platen, with successive layers bound together, then cured in an oven before post-processing. This technique enables the creation of intricate designs [98–102]

Laser Powder Bed Fusion (LPBF) has been extensively studied for fabricating W and its alloys. This technique for refractory alloys translates into selective laser melting (SLM) because of the high melting points of these metals [110]. LPBF (Figure 1a) [111] uses high-energy laser beams of 10^2-10^3 W (normally below 1000 W) [79,80,116], which result in pronounced spatial temperature gradients of about 10^6–10^7 °C/mm. Typical beam sizes are approximately 30-200 μm [80,116] and melt pool sizes about 100 μm [91,96]. The cooling rates are usually about 10^5-10^7 °C/s [80,116]. However, LPBF suffers from a major challenge: cracks forming, especially at grain boundaries. This happens because of three factors: rapid cooling creating thermal stresses, high stresses (von Mises) exceeding a critical point (DBTT), and oxygen trapped at the boundaries during the coalesce of the particles [38,48,82]. Nevertheless, SLM-fabricated W materials can achieve relative densities of 95% to 98.71% [49,66,73]. Advancements like femtosecond fiber lasers can potentially improve W AM with this technique [37]. Using the double melt strategy during AM processing also improves W densification [65]. SLM has the potential for integration with other techniques (such as infiltration) to achieve higher density in additively manufactured W parts [38,79].

Laser Directed Energy Deposition (laser DED), another AM method, has the distinction of directly adding energy during processing. This technique (Figure 1b) [112] uses even higher energy laser beams of 10^2-10^4 W [91,116], or more typically between 600-4000 W [80]), and a typical beam size of about 10^2–10^3μm [80,116] that results in spatial temperature gradients of (10^4–10^6 °C/mm) [80,116]. The cooling rates are approximately 10^2-10^5 °C/s [80,116], and usually closer to 10^4 °C/s [38]. In L-DED, the relationship between molten pool size and powder flow is crucial (Figure 1b) [28]. Although an increased laser energy can widen the molten pool, when the molten pool exceeds the flow of the powder, it can result in the reduction in the percentage of W entering [26]. This method is favored for manufacturing larger W parts than in EBM and LPBF-SLM [26]. However, challenges arise in managing surface roughness [89] and the formation of intermetallic compounds due to L-DED high energy inputs [50]. There remains a growing interest in laser DED for W alloys because it can produce materials with higher relative density compared to LPBF. This improved performance is credited to the technique's larger laser spot size [30,50].

Electron Beam Melting (EBM) (Figure 1c) [113] is a prominent AM technique for W. This method employs an electron beam as its primary heat source, which is manipulated through an electromagnetic lens, as detailed in Galati [81]. In comparison to laser-based AM methods, EBM offers a higher power level of 10^2-10^3 W [80,116], with typical values between 1000 to 3000 W [51,79,82]. With a beam size of 10^2 -10^3 μm [80,116], and scanning speeds approximating 10-10^3 mm/s [116], typical cooling rates of approximately 10^3-10^4 °C/s [80,91,116] can be achieved. This increased power is responsible for a relative density close to 99.5% in W materials [51]. EBM requires a high vacuum level post He/N_2 purge due to electron travel [51,82], and its processing window is depicted with scanning speed and current (or current density; Figure 4a) [51,79]. With appropriate preheating, EBM can address cracking issues in AM for W materials [51,80,81], with many promising results from EBM-fabricated W being reported [51,79,80]. EBM has also been adapted for W surface treatment to enhance quality, due to its controlled beam size and thermal influence [88]. Despite the advantages

 doi:10.20944/preprints202406.1108.v1

of EBM, challenges in its use that include complexities associated with electron focusing and the need for maintaining a high vacuum remain [51].

Laser Melting Deposition (LMD): This technique (Figure 1d) [114] like SLM, offers near-net-shape manufacturing capabilities from digital designs [91–97]. The high-energy laser beam of about 10^2-10^3 W [91,96] rapidly heats and cools powders, which reduces microstructural coarsening duration. However, while SLM-processed W materials show fusion deficiencies and non-uniform W particle distribution (despite powder preheating) that lead to brittleness, LMD, with its larger melt pools (about several mm) and reduced cooling rates of 10^3-10^4 °C/s [80,91,96,116], promotes W particle rearrangement and reduces porosity [92–95]. Tungsten heavy alloys (WHAs) with W contents up to 90 wt.% and with superior mechanical properties can be fabricated using LMD [97].

Binder Jet Additive Manufacturing: In the AM method of binder jet printing (Figure 1e) [115], a flowable powder is laid onto a build platen, followed by the selective deposition of a polymer adhesive in the shape of the intended part. After each layer, the platen descends, a new powder layer is spread, and the procedure is repeated. These layers are adhered together to create the targeted component. Once the printing is finished, the powder build box undergoes a heating process in an oven to solidify the adhesive [98–102]. The green body is subsequently separated from the surplus powder for further processing. Then the part undergoes dewaxing and sintering, similar to a standard compacted W component. This binder jet printing approach offers the capability to conceive and fabricate intricate designs that are difficult or unfeasible to manufacture via machining or other fabrication techniques. Tungsten heavy alloys with a relative density of 99.7% have been obtained via this method [98]. Investigating improvements to this technique is a promising avenue for future research on the AM of W and other refractory alloys that should be rigorously pursued.

The choice of an AM method for W materials depends on several factors including the material type, post-processing needs, geometric accuracy, cost, surface finish, and property requirements [52,80].

In subsequent sections, we will discuss AM of W-based materials, which includes pure W, W alloys, and W composites. We begin by examining the factors and processing strategies involved in the AM of unalloyed W. We next highlight methods to address the challenges related to processing and properties. Following this, we discuss additively manufactured W alloys and composites, presenting alloying strategies and the role of dispersed ceramic phases (in the W composites) on AM processing, and the resulting properties of W alloys and composites.

3. Additively Manufactured Unalloyed Tungsten: Challenges, Determining Factors and Mitigating Strategies

3.1. Problems and Resolutions in Brief

The remarkable properties of unalloyed W, including its exceptional melting point and high thermal conductivity, make it highly desirable in different applications. However, problems associated with the AM of W still need to be overcome. Fortunately, many studies in this area have been conducted that offer a solid foundation from which future improvements can be made to accelerate the development of high-performance W and its alloy from AM. This section will briefly introduce key challenges and look at their potential solutions (Table 2).

The mechanical properties of additive-manufactured unalloyed W, particularly its elongation, tensile strength, and fracture toughness, often fall short of expectations. Fortunately, researchers have found ways to significantly improve these properties through targeted alloying, the inclusion of ceramic reinforcements, and optimizing the parameters used during the AM process itself [68].

Tungsten is also inherently brittle due to its high Peierls stress that stem from its BCC crystal structure and weak grain boundary cohesion. The ductility of W can be improved through appropriate alloying, which improves the stacking fault energy (SFE) of the microstructure to enhance the slip mechanism [79]. The inherent brittleness of W is further exacerbated by its high ductile-to-brittle transition temperature (DBTT), thermal stresses, and oxygen-induced grain boundary issues, all of which led to cracking during the AM process. While strategies like alloying,

 doi:10.20944/preprints202406.1108.v1

incorporating carbide/oxide reinforcements, and process adjustments have shown some promise in improving the ductility of additively-manufactured W, further studies are needed to completely eradicate these cracking problems [40,57,68].

Another problem stems from the confluence of W's high melting point, low laser absorptivity (< 70 % in LPBF-SLM), and high viscosity, making it difficult for powders of W and alloying elements to properly melt and fuse during the printing process. Furthermore, the AM process can be plagued by phenomena like balling, where molten material forms spheres instead of adhering properly. Fortunately, the selection of W powders with improved laser absorption and optimization of processing parameters can mitigate these issues [49,57,59,60,62,70,72,117]. Optimizing process control parameters, particularly laser power and scan variables, has been shown to be instrumental in achieving better densification of W parts [49,57,60,118].

Tungsten's propensity for oxygen poses another challenge, as it leads to the formation and incorporation of tungsten oxide and subsequent hot cracking during AM. There are limited options for mitigating the oxidation of W during AM, including the use of high-quality starting materials, establishing better processing atmospheres, and using specific alloying combinations [68].

Table 2. A concise overview of the primary challenges, governing factors, and potential or attempted mitigation strategies in AM of W.

Challenges	Possible Strategy/Developments to Tackle the Challenge	Reference
The inherent brittleness and low ductility of W stem from 1) the high Peierls stress of its BCC crystal structure and, 2) weak grain boundary cohesion	Requires appropriate alloying to increase stacking fault energy for easier slip, and microstructural optimization.	[79]
High melting point, significant laser absorptivity (< 70% for SLM), pronounced viscosity, densification, porosities, balling, and deformation	Use of smaller, spherically shaped W powders to enhance laser absorptivity; Adjusting processing parameters to influence outcomes like defects, densification, and grain structures. Optimizing parameters like power and volumetric energy density have been found pivotal for improved W densification.	[49,57,59,60,62,72,91,118]
Oxygen affinity and tungsten oxide segregation lead to hot cracking	Better quality starting material (powder, wire) production, optimized processing atmosphere, alloying.	[68]
Cracks due to: W embrittlement and high DBTT, thermal stress-induced, difficult-to-control crystallization, and oxygen-induced cracking along the grain boundaries	Adjusting laser speeds and reducing grain sizes; Techniques to adjust laser speeds and reduce grain sizes showed some positive results but did not completely resolve the issue. Scanning strategy optimization: speed, rotation, remelting	[32,38,40,57,64,68]
Mechanical property issues (tensile strength and limited fracture toughness) especially in SLM-fabricated W	Alloying, introduction of reinforcements, process adjustments.	[68]

3.2. High Melting Point, Related Challenges and Controlling Strategies

 doi:10.20944/preprints202406.1108.v1

Tungsten's intrinsic high melting point, while invaluable for high-temperature applications, can result in pronounced thermal gradients during AM. Rapid heating and cooling cycles lead to thermal distortion, significant residual stresses, and crack initiation. This compromises the mechanical integrity of the printed components. Furthermore, W exhibits high thermal conductivity. In AM, this causes rapid heat dissipation, complicating the sustenance of the molten state, leading to partial melting and inconsistent fusion. These characteristics can influence the resultant component's microstructure and mechanical properties [48,60,61,72,86]. In the case of alloyed W, evaporation of low melting point elements can also be a challenge. Working at elevated temperatures also demands more of AM machinery, leading to heightened maintenance needs and increased costs [80,119]. Concurrently, the susceptibility of W and its alloys to oxidation increases at high temperatures, often leading to surface oxide formations that undermine material performance [68].

3.2.1. Melting

Melting behavior is integral to the AM of W, often serving as a key factor that defines its AM processing window. Direct melting of W is notably difficult, as the volumetric energy density required to melt W exceeds 8.595 J/mm^3, with the linear volumetric energy density at least 0.42 J/mm [57,79]. Such strict criteria lead to many partial melting situations, making it difficult to fabricate high-quality parts [71]. Tungsten material particle size and morphology, layer thickness, heat source power, volumetric energy density controlled by scanning variables and strategies, melting behavior, and interfacial characteristics are all important in the melting of W during AM processing.

3.2.1.1. Particle Size and Morphology

Tungsten's inherent properties necessitate the modification of its powders. These adjustments are needed to improve morphology, ensure uniform size, maximize laser absorption [45], and enhance surface conditions. Techniques such as the utilization of radio frequency plasma have been employed for these modifications [45,46]. The modifications are critical for powder flowability and to achieve the desired density [46]. Zhang et al. studied the influence of particle size on laser absorptivity [72], finding absorptivity to be higher when the powder bed was on a substrate as a result of incident laser rays entrapment. As an example, a 5 μm powder natively had 0.53 absorptivity but this increased to 0.603 on a stainless-steel substrate. Larger particles reduce absorptivity and fine particles improve printability. However, given the cost and limited availability of fine powder sizes, Wang et al. [45] explored an alternative approach to enhance W powder absorptivity. They managed to transform irregularly shaped powder particles into near-perfect spheres (close to 100% sphericity) using radio frequency (RF) induction plasma. These spherical particles were significantly smaller (average size of 31.5 μm) compared to the raw powder (average size of 56.8 μm). This transformation resulted in a significant increase in absorptivity, exceedingly not only the raw powder (as shown in Figure 2) but also exceed the values predicted by Zhang et al. [72]. Very fine particles with an average size of 17.3 μm were used to successfully obtain continuous tracks without cracks [48]. However, it is important to note that studies have not established a direct correlation between particle size and achieving crack-free tracks of pure W.

 doi:10.20944/preprints202406.1108.v1

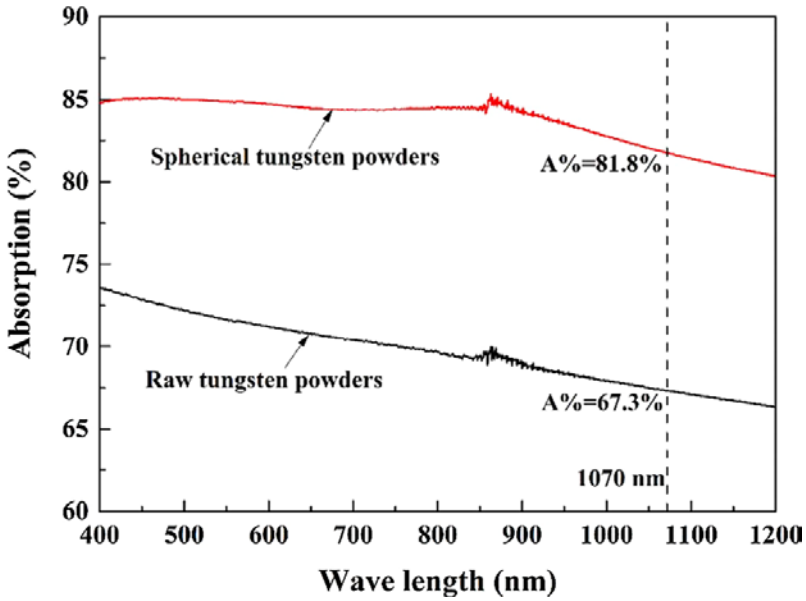

Figure 2. Comparison of absorption properties between non-spherical (raw) and spherical tungsten powders (RF treated) [45]. Reproduced with permission from Elsevier.

3.2.1.2. Power, Volumetric Energy Density, Layer Thickness

Volumetric energy density (VED) is a pivotal parameter in AM design, as it plays a decisive role in defining the processing parameters. This can be mathematically represented in Equation (1), where the volumetric energy density (E) is expressed as follows [120,121]:

$$E = P/(v \times s \times t) \quad (1)$$

where P is the laser power, v the laser scanning speed, s the hatch spacing, and t the layer thickness.

Sidambe and Fox [122] as well as Sidambe et al. [55] investigated the impact of VED on the relative density of manufactured components. Both studies found relative density to increase with higher VED, although the latter reported even higher relative density values at the same VED (Figure 3a). Guo et al. [60] and Hu et al. [61] examined the impact of VED on relative density and hardness using spherical particles. They found that increasing VED led to increased relative density and decreased pore size to achieve a maximum relative density of approximately 98.3%. Microhardness also increased with higher VED, reaching values of 474 Hv [60] and 430 Hv [61]. Other studies on LPBF-SLM, however, reveal the complexity of the influence of VED and laser power. Yamamoto et al. investigated how laser power, scanning speed, and hatch spacing affect the density of 3D printed tungsten cylinders [69]. The parts printed from pure polyhedral tungsten powder at a preheating temperature of 35°C showed that higher laser power and wider hatch spacing led to denser parts, matching the results from those from Rebesan et al. [56]. Plotting the VED against relative density showed the highest relative density reached to be 98.58% at VED of 411 J/mm^3 (P = 370 W, v = 500 mm/s, h = 90 μm, t = 20 μm; Figure 3b). This VED trend differed from those of Guo et al. [60] and Enneti et al. [70], who reported increasing relative density within the VED range. This difference highlights the uncertain role of VED in relative density estimation. Manufacturing 3D parts is complex, with hatch spacing and scanning strategy affecting part integrity, porosity type, and thermal history for each layer. Thus, interpreting these trends requires a full understanding of each study's parameters and specific porosity characteristics [69,77]. Wen et al. [49] studied the fabrication of W cubes with varying laser power, scanning speed, and hatch spacing. They found the use of low laser power to result in dense, high-relative-density cubes due to the laser's impact on melt pool temperature. Increasing the line (laser) energy density (LED) led to warped morphologies, which were eliminated with further LED increase due to stronger interlayer bonding. Cracks were observed but reduced with higher scanning speed, reaching a maximum relative density of 98.71% at 200 mm/s scanning speed.

 doi:10.20944/preprints202406.1108.v1

For W materials, a higher volumetric energy density and subsequent higher processing temperature may reduce the resultant residual stresses due to enhanced annealing effects [79,123]. This reduction in residual stresses might be why using EBM generally leads to a reduced cracking probability in W materials when compared to using LPBF [82]. Extremely high volumetric energy densities (e.g., > 300 J/mm^3) are not necessarily beneficial (Figure 3c) [38,69,124]. Achieving high density in 3D-printed tungsten parts can be challenging due to several factors. One issue is unstable laser melting. The intense laser beam can create deep holes, called keyholes, that don't fully solidify, leaving air pockets (porosity) throughout the part [38]. Another problem arises from using too much laser power. Excessive melting disrupts the molten metal pool, trapping air bubbles and reducing density [51]. Powder application can also be problematic. If particles don't flow smoothly into the melt pool but instead stick to the edges, they create voids and hinder densification [51]. Finally, tungsten's high melting point presents another hurdle. Some elements that evaporate easily (volatile elements) may vaporize during the printing process, leaving behind tiny holes that contribute to lower density [79,80].

The work of Wang et al. on the L-DED processing of W also found the relative density of the obtained parts to increase with VED (Figure 3d) [94]. In their study on EBM processing of unalloyed W, Dorow-Gerspach et al. investigated the impact of linear energy density (LED) variations achieved by varied the power and speed of the electron beam to investigate its effect on cubic samples [84]. These experiments were carried out at a substrate preheating temperature of 1000°C., in which they achieved a high relative density of 99.5% but observed cracking in all fabricated cubes. While increasing electron beam energy led to decrease in relative density, it also resulted in a decrease in crack density (Figure 3e), highlighting the trade-off between densification and structural integrity in this AM process [84].

High energy inputs in AM processes that include LPBF-SLM affect the molten pool due to the Marangoni effect. The severity of this effect is directly proportional to the laser energy input [57,125,126]. This effect can drag gas into the molten pool, leading to pore formation upon solidification. Excessive laser energy density, especially at lower scan velocities, can also result in molten pool instabilities, yielding a rough track [48]. As SEM images showing the typical surface morphologies of scanning tracks at different laser powers in the AM processing of W (Figure 4a-e [48]) indicate, an optimal laser power can result in a regular flow front and no cracking (Figure 4b).

Properly controlling the melting behavior can lead to several advantages. High energy input can enable elements with lower melting points to be mixed. This behavior, governed by Marangoni convection, can enhance interfacial bonding during AM [48,110]. Stable molten pools facilitate the growth of complete columnar crystals in additively manufactured W parts [51]. Techniques like EBM can introduce remelting during AM, annealing the built portion of the W parts and reducing crack susceptibility [82].

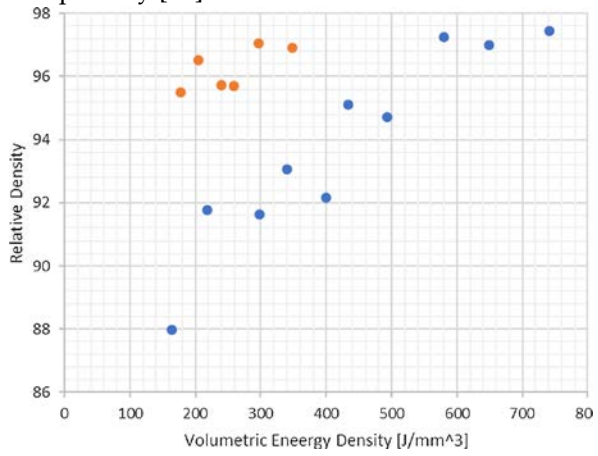

(**a**)

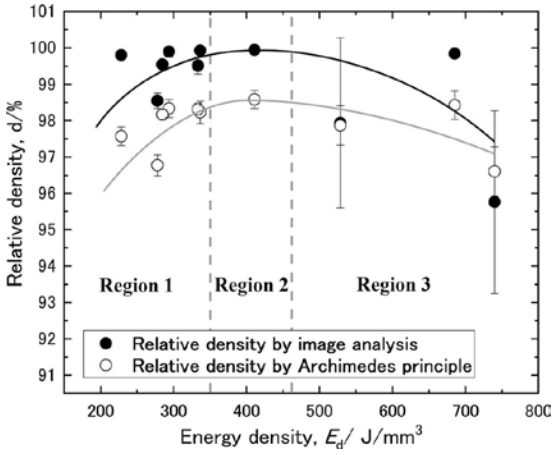

(**b**)

Preprints.org (www.preprints.org) | NOT PEER-REVIEWED | Posted: 17 June 2024 doi:10.20944/preprints202406.1108.v1

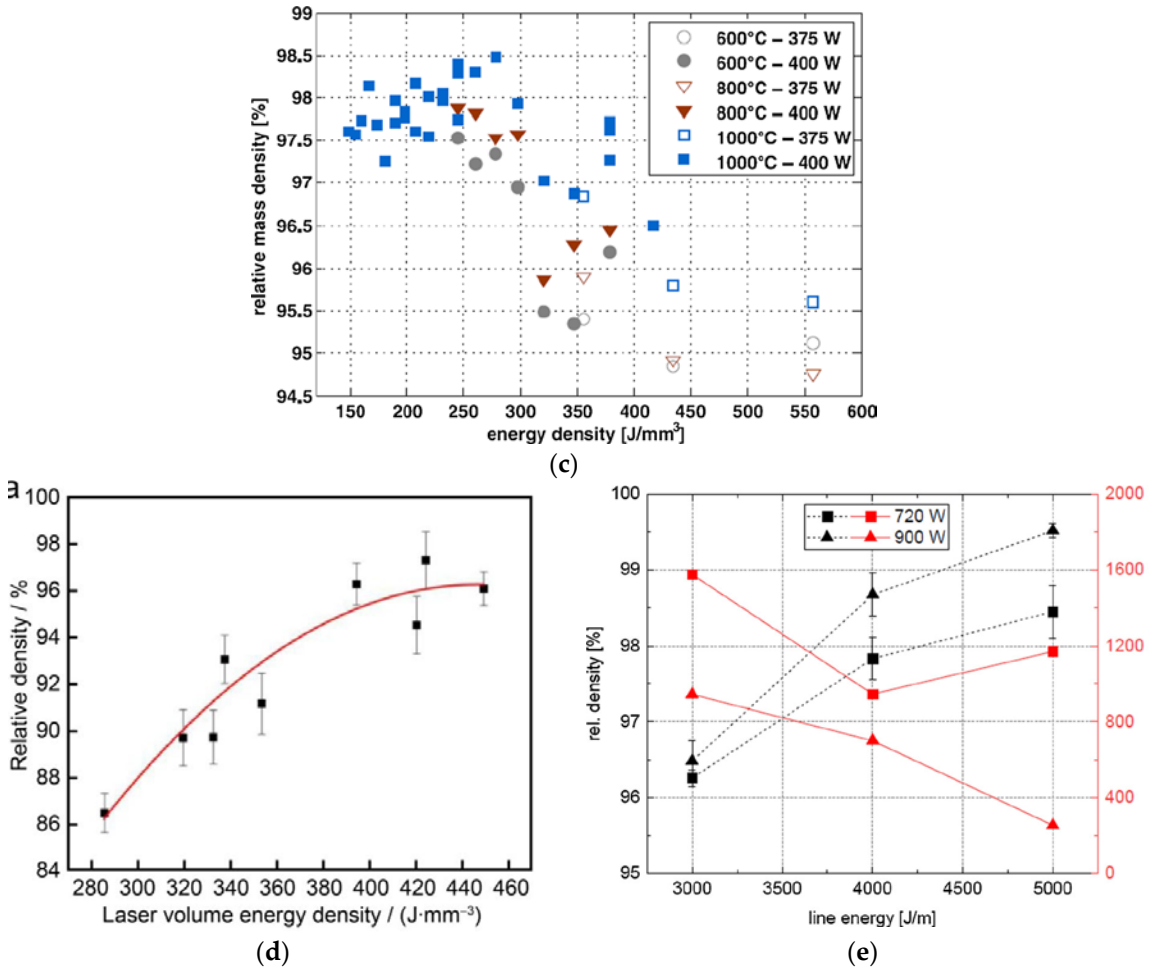

Figure 3. a) the relative density of SLM-fabricated W cubes by Sidambe and Fox [122] and Sidambe et al. [55], b) influence of Volumetric Energy Density (VED) on the density of pure tungsten parts made with Laser Powder Bed Fusion (L-PBF) [69], c) influence of substrate preheating temperatures onrelative mass density of tungsten [38], d) relationship between laser energy density and density in tungsten-nickel alloy (W-15Ni) parts created using Directed Energy Deposition (DED) [94], e) influence of Linear Energy Density (LED) and electron beam power on the relative density of tungsten parts made with Electron Beam-Powder Bed Fusion (EB-PBF) [77]. Data and figures were reproduced with permission from Elsevier.

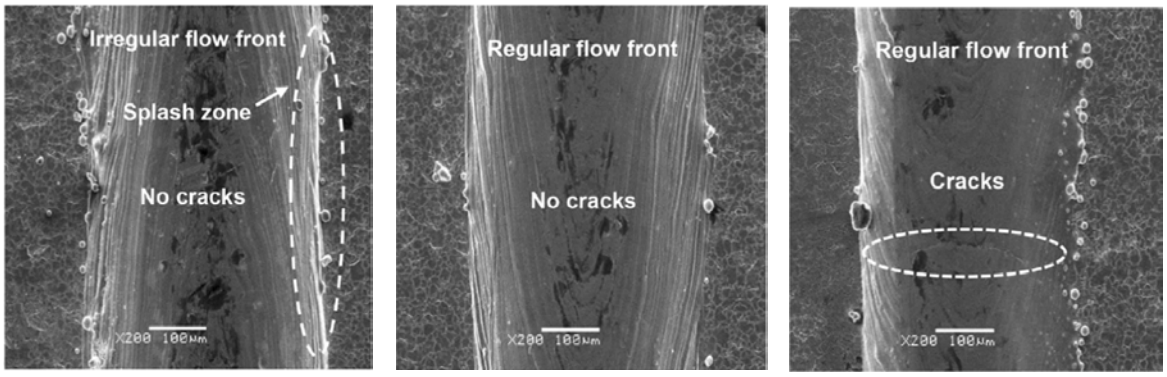

 doi:10.20944/preprints202406.1108.v1

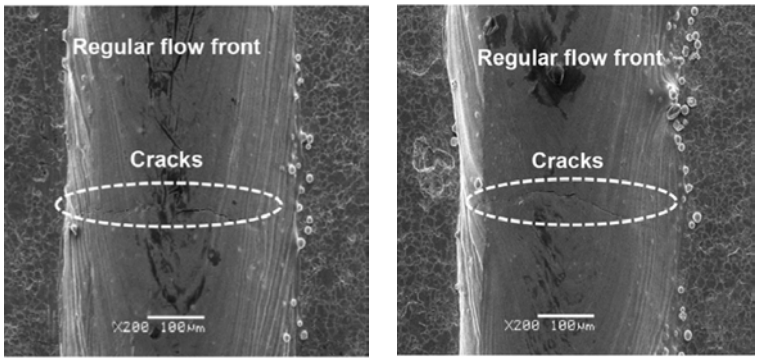

(**d**) (**e**)

Figure 4. SEM images showing surface morphologies of scanning tracks at laser power of (a) 250 W, (b) 300 W, (c) 350 W, (d) 400 W, (e) 450 W, the scanning speed is 200 mm/s [48].

Another parameter affecting melting in AM processing is the layer thickness as indicated in Equation (1). The comprehensive review by Marcos et al. indicates that reducing the layer thickness in powder bed melting processes requires less energy to melt the powder, resulting in continuous conduction mode tracks at lower energy input levels [77].

3.2.1.3. Other Scanning Variable and Strategies

The scanning pattern plays a critical role in determining the thermal history of processed W materials, offering a flexibility suitable for a variety of applications. This flexibility represents a unique advantage of AM over traditional manufacturing techniques. Table 3 offers an overview of scanning variables and strategies employed in in AM of W. The localized differences in material properties can be ascribed to the focused energy input from electron or laser beams or other energy sources that determine the thermal history a point experiences [79]. In the EBM process, for example, one can witness multiple instances of melting and re-melting at a single scanning point [82]. In AM for W materials, different scanning patterns have been explored. A 67° rotation between layers randomizes grain orientation, reducing the ladder-shaped grain structures which are potential crack-formation sites [40]. While many studies adopt a 67° rotation to minimize scan alignment, others use rotational angles of 45° or 90° [32,38,46]. Remelting, which is scanning a track multiple times before recoating, combined with rotation, curtails the formation of columnar grains and reduces longitudinal cracks, resulting in smaller grain sizes and reduced surface roughness [40,64,80].

EBM, as a method, is not left behind, adapting flexible bidirectional scanning tactics to home in on the best print quality [51]. Wang et al. [40] investigated crack development in laser powder bed fusion of unalloyed W. They studied three scanning strategies: parallel, 67° rotation, and remelting with 67° rotation. Matching scan tracks between layers resulted in consistent crack growth along the build direction. Rotation between layers reduced crack propagation, while remelting did not effectively reduce cracks but instead promoted thermal fatigue crack growth [40].

Diving deeper into the nuances of pattern design and its influence on additively manufactured W materials, studies have highlighted the quantifiable effects of specific pattern parameters. Hatch spacing, interestingly, is responsible for a mere ~7% fluctuation in the final W densification [79]. Point distance is another crucial factor, having a profound impact on the AM relative density for W materials. Wang et al. [62] and Huang et al. [127] studied the influences of point distance and hatch spacing on the relative density of W achieved when pulsed (Figure 5a), and continuous lasers were used (Figure 5b,c) respectively. By adjusting these parameters, different melting strategies can be deployed, presenting an opportunity to oversee and regulate re-melting sequences to ensure that they sidestep randomness [65].

 doi:10.20944/preprints202406.1108.v1

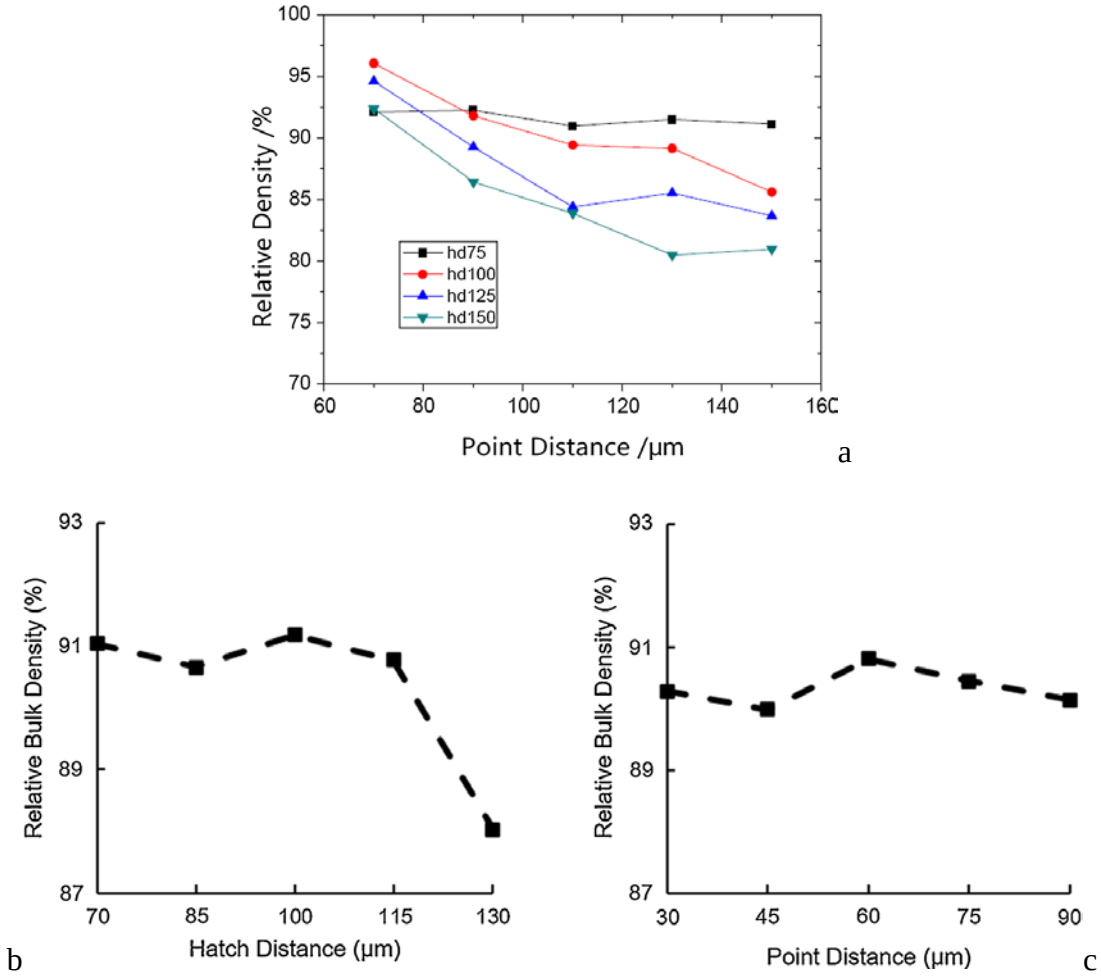

Figure 5. Influence on the relative density of manufactured W cubes due to the interaction between hatch spacing (hd) and point distance with input parameters of : a) pulsed laser power of 400 W and exposure time of 100 μs [62], b) and c) at a laser power of 40 W, layer thickness of 50 μm, and exposure time of 300 μs [127]. Reproduced with permission from Elsevier.

Scanning speed is yet another dominant factor, accounting for a significant ~75% variation in W densification within the SLM process [70,79]. In their study, Ren et al. [36] examined how morphology of W single tracks can be influenced by laser power and scanning speed. These single tracks were created using powder particles ranging in size from 5 to 25 μm and were printed onto a stainless-steel substrate preheated to 200°C. Establishing a processing map based on the surface characteristics of the single tracks (Figure 6a), allows different regions where one can observe regular tracks, irregular tracks, or instances of balling to be delineated. Rebesan et al. [56] explored how adjusting the laser scanning speed and spacing between hatch spacing affects the density of tungsten parts made using Selective Laser Melting (SLM) at a power of 170 W and spherical particles (Figure 6b). This approach yielded impressive results, achieving high relative densities of 96.4% to 99.3%. However, both longitudinal and traverse cracks were observed within the finished parts. Enneti et al. took a different approach, with the laser power was kept at 90 watts, volumetric energy density (VED) of 1000 J/mm³ and the base plate preheated to 80°C [70,118]. With these settings, densities ranging from 60% to 75% was achieved. Li et al. [128] examined the impact of process parameters (laser power P, scanning speed v, hatch spacing h) on the density of as-LPBF bulk W parts, achieving a maximum relative density of 98.31%, and creating process maps (Figure 7). Here, there was a direct correlation between laser power and density (Figure 7a), with hatch spacing and scanning speed having minor effects (Figure 7b,c). High densities (>98%) were consistently attained with 250–300 W power, 0.08–0.1 mm hatch spacing, and 0.03 mm layer thickness, offering valuable insights into

 doi:10.20944/preprints202406.1108.v1

process optimization. Xiong et al. [64] used image analysis to measure density and established process parameters for achieving high-density W coupons. They achieved densities of 97.3% to 98.1% with laser powers between 250 and 300 W and scanning speeds of 400 to 500 mm/s. Dong et al. experimented with different factors to see how they affect the quality of 3D-printed tungsten parts [129]. They printed the parts using a preheating temperature of 100°C and used irregularly shaped particles (polyhedral) for the material. They found that parts printed under a nitrogen (N_2) atmosphere achieved higher density, hardness, and overall strength compared to those printed under argon (Ar) atmosphere. Furthermore, using higher laser power and slower scanning speeds led to denser parts. However, if the scanning speed was too high, it caused the material to ball up (bunch together) and resulted in surface pores.

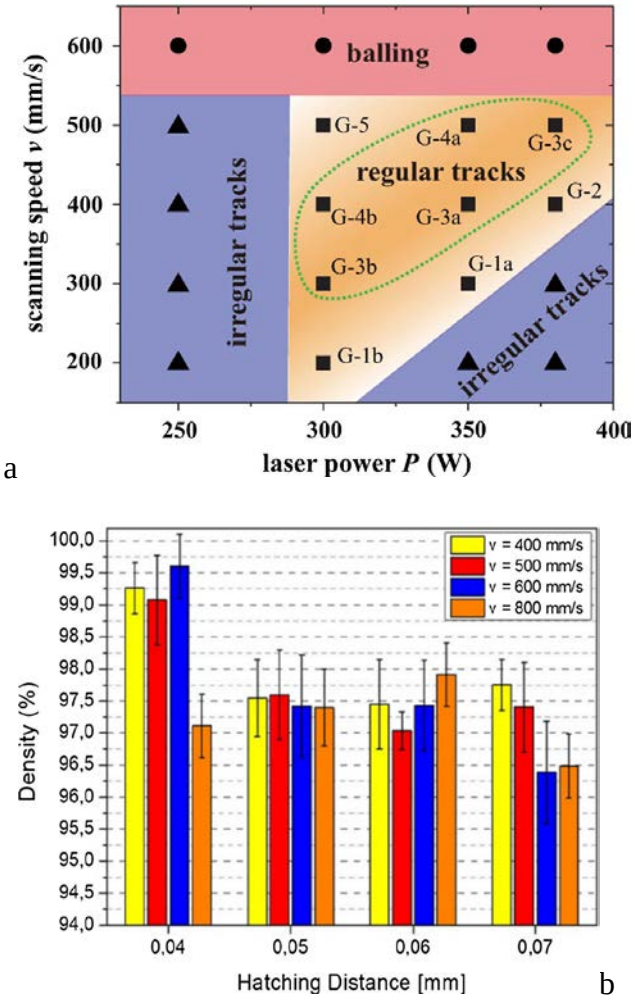

Figure 6. a) L-PBF processing map for unalloyed W [36], b) influence of hatch spacing and scanning speed on the relative density of pure W samples. The laser was maintained at a power of 170 W and substrate preheated 80°C [56]. Reproduced with permission from Elsevier.

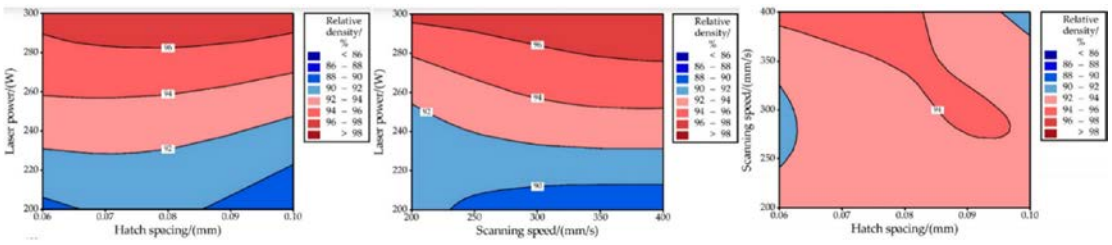

 doi:10.20944/preprints202406.1108.v1

Figure 7. Process maps for W; (a) laser power vs. hatch spacing; (b) laser power vs. scanning speed; and (c) scanning speed vs. hatch spacing, [128].

In examining the role of scan track design, we find it to play an important role in pattern design, especially in upholding the quality of SLM-printed parts [79]. Here, parameters like the single scan track width, and hatch spacing can be adjusted. Within SLM, the overlap rate is devised in line with these two parameters, serving as an analytical tool to gauge conditions across multiple scan tracks. Previous studies have underscored a non-linear relationship between scan track characteristics, which is dictated by overlap design choices, and the eventual densification of W material. This points to the existence of an optimal overlap rate that balances these parameters [36].

Table 3. An overview of scanning variable and strategies employed in AM of W.

Scanning Parameters	Details	Reference
Volumetric Energy Density	-**Volumetric Energy Density:** - ***Increased power*** in AM affects the molten pool via the Marangoni effect, with the severity proportional to laser energy. - can introduce gas, causing pore formation and pool instabilities, resulting in rough tracks - enhances the densification of manufactured parts - reduces residual stresses via annealing - volumetric energy density relates to pattern design. - ***Extremely high energy densities*** (> 300 J/mm3) have drawbacks: more porosity, excessive fusion risks, disrupted melt pools with stuck powder particles, vaporization of volatile elements due to W's high melting point. These challenges impact printed part quality. ***Controlled melting has benefits:*** allows mixing of low melting point elements and improves interfacial bonding. Promotes growth of full columnar crystals in W AM parts. Techniques like EBM anneal W parts, decreasing cracks.	[38,48,51,57,69,79,80, 82,94,110,123–126]

 doi:10.20944/preprints202406.1108.v1

	- **Direction & Angle:** - EBM process allows multiple melting and re-melting at a single scanning point. - 90° alternating bidirectional scanning in SLM. - 67° alternating bidirectional scan.	
Scanning Variables	- **Speed:** scanning speed affects ~75% of W densification variation in SLM. - **Hatch Spacing:** affects ~7% of W densification variation. - **Scan Track Width (w):** a parameter in SLM. - **Overlap Rate (φ):** relationship between scan track characteristics and final W material densification is non-linear. Optimal overlap rate exists.	[36,38,46,51,65,70,79,82]

3.2.1.4. Wetting Behavior and Interfacial Characteristics

Interfacial design and W wetting behavior at multiple scales is pivotal for producing high-quality components via AM especially because of their influence in reducing crack initiation and propagation, and on mechanical properties (Table 4).

Microscopic wetting behavior involves the internal heterogeneous boundaries within the 3D-printed W materials. W is not easily wettable by most metals at lower temperatures (below 2000°C). The temperature-dependent wettability of W has been a focal point for many researchers [79,130]. Muramatsu et al. [110,131] underscored the significance of the heterogeneous interface, especially when considering the broad temperature range covered in AM [110,130,132]. To enhance the AM quality of W-based materials, researchers have introduced small quantities of transition metals like Ni and Fe. These elements reduce the activation energy required during the sintering of W, accelerate W diffusion, and provide improved wettability to facilitate the AM process [79,110].

On the other hand, macroscopic W-material/substrate interfacial wetting and reaction involve the interfaces between the substrate and the W material to influence the final quality of the AM product. Stainless steel interlayers, containing nickel, have been employed to improve the adhesion between W and other alloying elements due to enhanced solid-state diffusion and grain boundary diffusion [110]. For better AM outcomes, substrates can be substituted with Ti-based alloys such as Ti–6Al–4V due to the enhanced thermodynamic compatibility between W and Ti [51]. Novel AM methods, like sandwich-structural printing sequences, have been developed for W materials, leading to better quality AM parts [133]. However, using such interlayers can lead to diffusion-induced secondary phases. Additionally, interactions with other elements might bring about unwanted reactions, such as the peritectic reaction seen between Fe and W during non-equilibrium solidification [93,110].

Table 4. An overview of W wetting behavior and interfacial phenomena at micro as well as macro scale in AM processing.

Category	Description	Examples & Developments	References
Microscopic Wetting Behavior	Concerns internal heterogeneous boundaries in 3D-printed W materials.	- Temperature-dependent wettability of W - Introduction of Ni and Fe to improve wettability and AM quality	[79,110,130–132]

 doi:10.20944/preprints202406.1108.v1

Macroscopic W-Material/Substrate Interfacial Wetting and Reaction	Relates to interfaces between substrate and W material, affecting AM product quality.	- Use of stainless-steel interlayers containing nickel - Substituting substrates with Ti-based alloys, e.g., Ti–6Al–4V - Sandwich-structural printing sequences for W AM - Risks of diffusion-induced secondary phases and unwanted reactions	[51,93,110,133]

3.3. Oxygen, DBTT and Micro-cracking

Oxygen, along with other interstitial contaminants like nitrogen and hydrogen, presents serious challenges in AM of refractory alloys (including W materials). Such contaminants, particularly oxygen, critically affect properties like the DBTT transition in W materials, with molten W being especially sensitive to oxygen [36,134–136]. This heightened sensitivity leads to adverse outcomes, including embrittlement, increasing DBTT, and decreased strength. Table 5 summarizes our current understanding of oxygen contamination for W in AM processing. Common sources of oxygen contamination include oxidized powder surfaces, residual oxygen in the chamber [68], and in the substrate due to high thermal energy inputs, suggesting that substrates may function as oxygen reservoirs [38]. The powders utilized in AM, owing to their vast surface-to-volume ratio, are notably prone to absorbing oxygen from their surroundings, further complicating this issue. Moreover, when W is exposed to oxygen at room temperature, it promptly forms an oxide layer within an hour [137]. Nagy and Humphry-Baker conducted a brilliant study [136] on oxidation of W and developed a W oxidation mechanism map to reveal the kinetics of W oxidation at the 600-1600°C temperature range (Figure 8). This can be useful in the AM of W materials. Under AM's elevated temperatures, oxygen can not only diffuse swiftly into the alloy but also react with W, resulting in intergranular cracking upon cooling [67,82,138].

Table 5. Current understanding about oxygen contamination in W in AM processing.

Factor/Parameter	**Details/Effects**	**References**
Contaminants in AM	Oxygen, nitrogen, hydrogen	[36,134–136]
Adverse Effects	- Embrittlement - Shifts in DBTT - Strength reduction - Cause cracking especially at high angle grain boundaries	[36,40,134–136]
Sources of Oxygen in W Materials	- Oxidized powder surface - Residual oxygen in the chamber - Substrates due to high thermal energy inputs	[38,68]
Oxygen Sensitivity in W Materials	- Molten W is sensitive to oxygen - Oxide layer formation (1 nm thick within an hour) - Potential for intergranular cracking upon cooling	[67,82,137,138]
Oxygen Control Techniques in AM	- Higher beam power - Enhanced volumetric energy density - Radio frequency induction plasma treatment	[45,82]

 doi:10.20944/preprints202406.1108.v1

Material Design for Reduced Oxygen Sensitivity	Introduction of alloying elements such as Ta to W	[67]
Important Studies and Findings	Oxidation mechanism map for AM applications exists	[136]

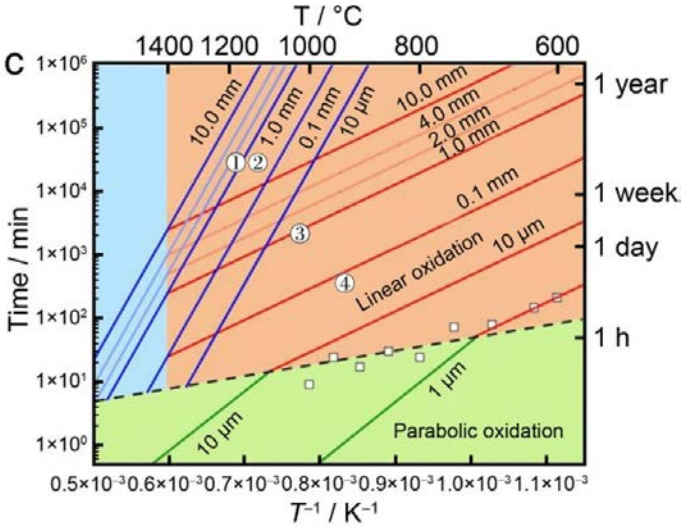

Figure 8. W oxidation mechanism map in the temperature range of 600-1600 °C and up to 2 years. Contours indicate the thickness of the metal oxidized. The parabolic, linear, and sublimation regions are shaded in green, red, and blue respectively [136]. Reproduced with permission from Elsevier.

Reducing oxygen levels during the AM process is paramount, as this will improve part quality by reducing the occurrence of cracks [68]. Emphasizing the significance of oxygen, even at reduced levels, W oxides can remain stable at up to 2000°C, potentially initiating cracks during rapid solidification [134]. To confront these challenges, researchers can turn to several strategies in many metallic systems. The use of inert gas environments, such as argon or helium, during AM offers a practical way to minimize contamination by isolating the alloy from potential contaminants. Additionally, enhancing powder handling and storage protocols – like the vacuum packaging of powders and handling under inert atmospheres – is another avenue being explored to eliminate contamination. Gas atomization under inert conditions stands out as an innovative powder production method, delivering powders with appreciably lower oxygen and nitrogen contents. Apart from inert gas environments during AM, post-processing techniques like hot isostatic pressing (HIP) can also be explored. Implementing techniques like using higher beam power and enhancing volumetric energy density can diminish the oxygen content and curb cracking [82]. The role of oxygen is not just restricted to the fabrication process but extends to preheating, underscoring the necessity for an oxygen-regulated environment [51]. Innovatively, as pointed out earlier, methods such as radio frequency induction plasma treatment have been deployed to manage oxygen levels effectively [45]. Furthermore, material design advancements, like introducing Ta to W, offer a promising avenue to counteract oxygen sensitivity [67]. To facilitate deeper insights, detailed studies to understand W oxidation have been undertaken, resulting in the creation of an oxidation mechanism map tailored for AM [136].

Crack nucleation and propagation in AM of W correlate with its high DBTT of approximately 200-600°C. Support for this comes from an observed delay between solidification and crack appearance using in-situ high-speed cameras reported by Vrancken et al. [43,54]. Cracks often propagate along high angle grain boundaries (HAGBs) [40], where the formation of cracks in the intergranular regions of SLM-fabricated W has been mostly observed. Such behavior is linked to W's grain boundary sensitivity to impurities, notably oxygen, found in amounts between 30-370 ppm in W powder [43,57]. While some researchers attribute cracks to tungsten oxide aggregation during solidification [40,56,60,61], persistent cracks at low oxygen levels indicate other possible influencing

 doi:10.20944/preprints202406.1108.v1

factors as well [43]. The role of impurities, including oxygen and hydrogen, on L-PBF W's brittleness has not been fully explored. High-speed in-situ SLM videos show cracking across W's DBTT, likely due to the increased von Mises stresses [43]. Such stresses from SLM may only be offset by cracking at impurity-contaminated grain boundaries [21,61]. An important study by Rebesan et al. on W specimens produced by the LPBF process revealed a high cracking tendency [56]. Two types of cracks were identified: longitudinal (along the melt-pool center) and transverse (perpendicular to laser-induced surface ripples). Longitudinal cracks are linear and 30-100μm long, while transverse cracks are shorter with an "S"-shape along grain boundaries (Figure 9). The extensive cracking results from thermal stresses during rapid solidification or recrystallization (Figure 10a), particularly below the DBTT. Micro-cracks that resemble intergranular hot cracking form due to nanopore aggregation at grain boundaries induced by boiling tungsten oxides (WO_x) in the melting pool (Figure 10b) [56].

Cracking in EBM W is comparable to SLM processed W, with their mechanisms still under debate. Solid-state cracks may arise from inelastic deformation near low-angle grain boundaries (Figure 11a), which is supported by EBSD data (Figure 11b) [82].

In L-DED, residual stress-induced cracking due to high thermal gradients and porosity are common challenges [80]. However, oxygen contamination and its contribution to microcracking is present in AM processing of W for all techniques.

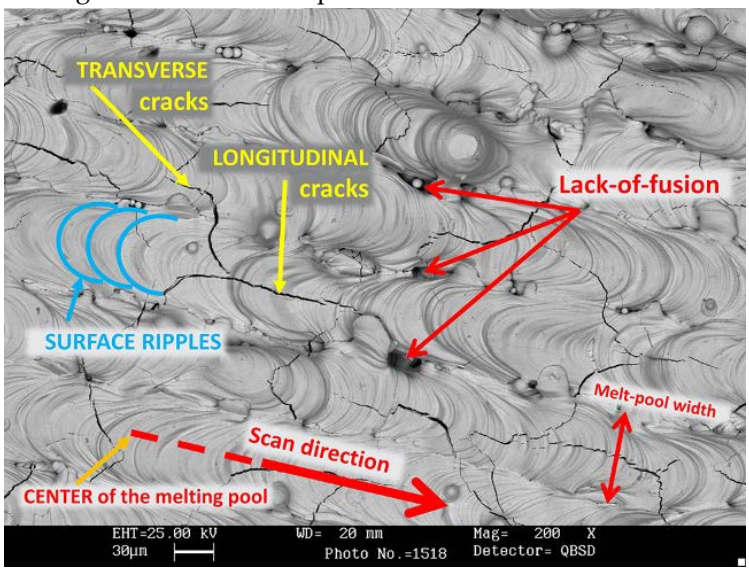

Figure 9. SEM image of details on surface morphology and cracks type in LPBF -W [56].

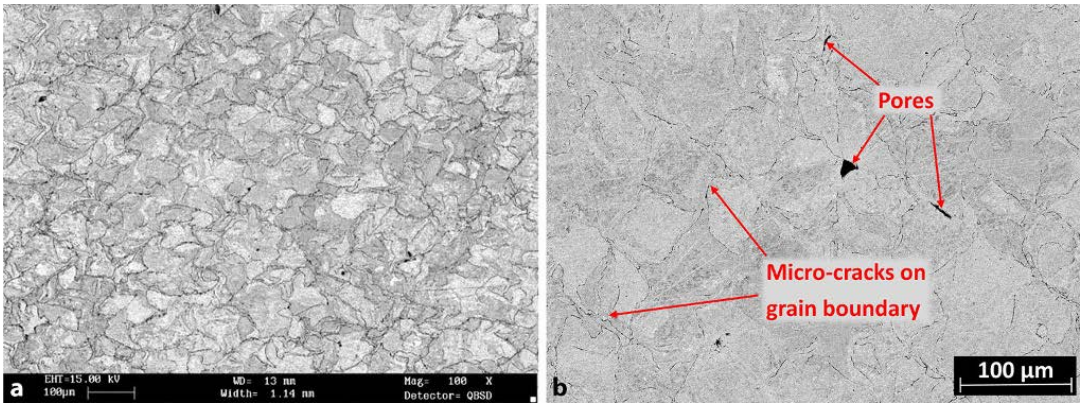

Figure 10. SEM images of a) W electrolytically etched AM W sample displaying a crack network; b) AM W sample displaying a magnification of grain boundaries, micro-cracks and pores, [56].

 doi:10.20944/preprints202406.1108.v1

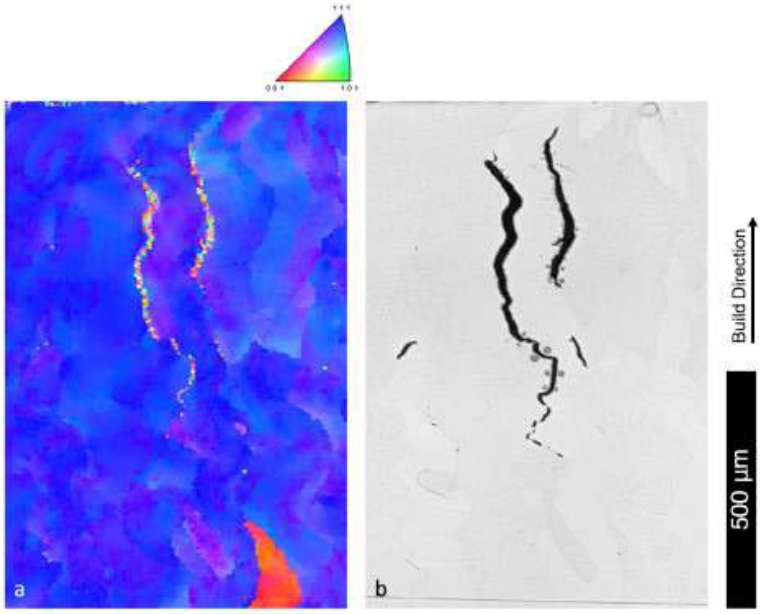

Figure 11. AM W section depicting a vertical crack at grain boundary shown in a) EBSD, where the crack appears as random unindexed pixels and b) optical image. Several small droplets of water are visible at the edge of the crack in the optical image [82].

3.3.1. Substrate Preheating

Utilizing a heated substrate plate in the powder bed AM process can potentially mitigate the problems posed by thermal gradients [38,57]. Preheating is an essential preparatory technique implemented before the actual AM process to optimize the material's structure and improve the results of AM. This method confers several advantages (Table 6). Firstly, it aids in the mitigation of built-up thermal residual stresses within the material to enhance its stability [123]. Moreover, by controlling the melt pool's cooling rate and the thermal gradient during solidification, preheating ensures improved material properties and formation. This is particularly critical for materials like W which have a high DBTT; preheating can potentially delay or even avert this transition [63]. Additionally, preheating can emulate the annealing process, refining W's microstructure [123] to produce parts with increased density and fewer microcracks. In some cases, preheating the substrate to temperatures approaching 1000°C has proven effective in achieving these outcomes [38].

Table 6. An overview of the effects and benefits of preheating in AM of W materials.

Preheating Effects	**Information/Description**	**Reference**
Purpose	Used before the process to enhance AM results	
Benefits		
- Mitigation of Stress	Reduces built-up thermal stresses	[118]
- Melt Pool Dynamics	Controls cooling rate and thermal gradient during solidification	
- Delay/Avoidance of DBTT	Delays or prevents DBTT, crucial for materials with a high DBTT like W	[63]
- Annealing Effect	Simulates the annealing process, refining W microstructure	[123]
- Enhanced Density & Reduced Microcracks	Increases part density and reduces microcrack formation, especially with preheating up to 1000°C in SLM, and more in EBM	[38,82]
Optimal Preheating Range		

 doi:10.20944/preprints202406.1108.v1

- Observation	Low preheating temperatures below 400°C are insufficient for microcrack mitigation of W materials	[32,51]
- General Findings	Higher preheating temperatures minimize high DBTT effects and enhance mass density of additively manufactured W parts	[38]
Drawbacks of Excessive Preheating		
- Recrystallization	Extremely high temperatures trigger recrystallization in material	[82]
- Grain Vulnerabilities	Larger recrystallized grains are prone to intergranular cracking, acting as pathways for cracks near grain boundaries	[79,135]
- Counter-productiveness	Very high preheating temperatures can be counterproductive	[79,82]

Elevating substrate temperature beyond W's DBTT decreases cracking likelihood, thereby improving the relative density of parts manufactured using AM with W. SLM processing at increased temperatures from 200°C to 1000°C reduced cracking. Such findings have been visually represented in the works of Muller et al. (Figure 12) [38], where they compare the microstructure of SLM-fabricated W with a substrate temperature of 200°C that includes grain boundary cracks (Figure 12a), to that of a SLM-fabricated W using a substrate temperature of 1000°C without cracks (Figure 12b).

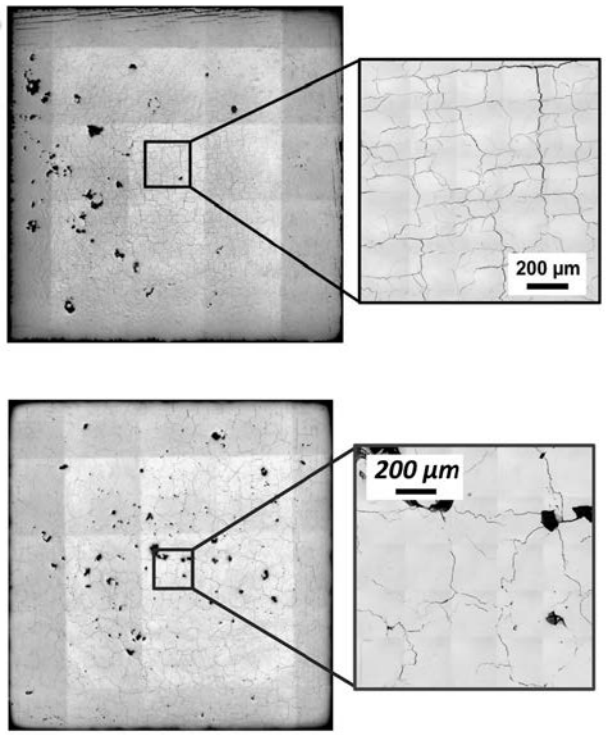

Figure 12. Effect of temperature on pure tungsten cubes: a) optical image of a cross-section at 200°C, b) optical image of a cross-section at 1000°C [38]. Reproduced with permission from Elsevier.

In another study, using ~850°C substrate heating led to minor cracking [51]. Other observations indicate that temperatures below 400°C are inadequate for preventing microcrack formation [32].

Vrancken et al. also showed that the exact temperature above which cracks in SLM-fabricated W are eliminated ranged from 500°C to 600°C. The crack mitigating effect of preheating persists when scaling up from a single scan track to a hatched area. Without preheating, a large crack network is formed (Figure 13a), whereas only small, isolated cracks are found using 500°C preheating (Figure 13b) [63].

 doi:10.20944/preprints202406.1108.v1

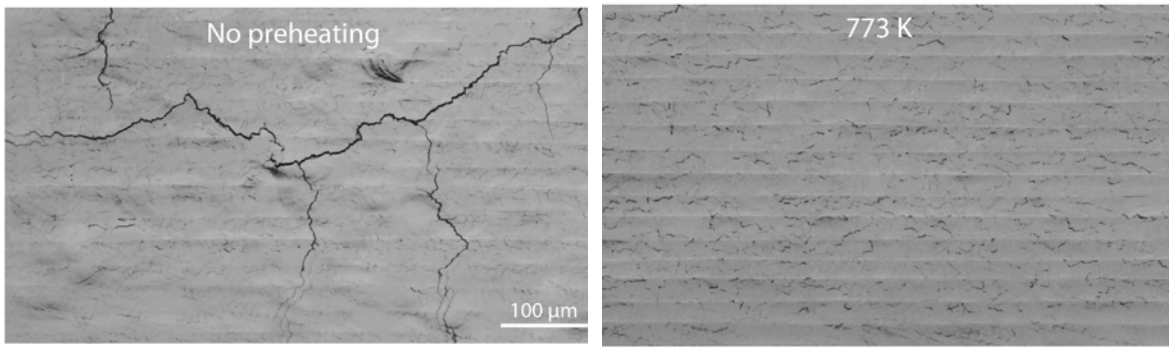

(**a**) (**b**)

Figure 13. a) Crack pattern of a 1 by 2 mm area scanned using hatch spacing h = 25 µm , and (b) absence of cracks in a 1 by 2 mm area scanned using 500°C preheating, both in SLM-fabricated W. [63]. Reproduced with permission from Elsevier.

Similarly in EBM processing of W, Ellis et al. observed a lower crack density at 1500°C (corresponding to preheating input energy of 735 J/mm^2) than at 1100°C (corresponding to preheating energy input of 325 J/mm^2)(Figure 14 a,b)[82]. This led them to postulate that the higher preheat energy suppresses cracking by raising the ambient temperature of the build [82].

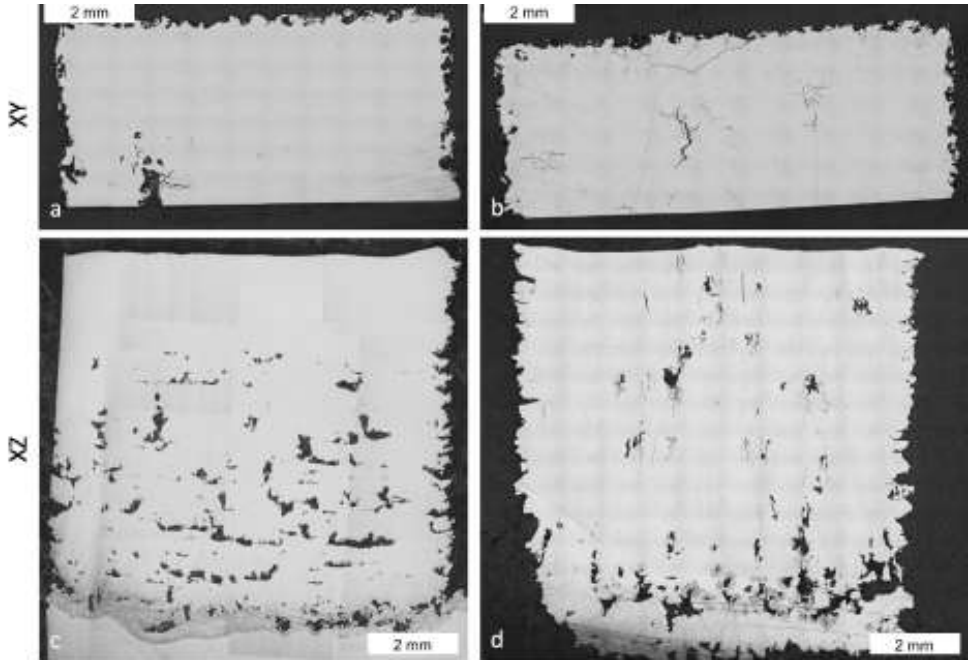

Figure 14. Two W blocks built with nominally identical melt parameters, a) and b) XY sections, approximate elevations 9 mm, c) and d) XZ sections, approximately at midline. The build shown in a) and c) did not crack, the build in b) and d) exhibited cracking, [82].

However, we must approach the issue of preheating with care. While the technique is beneficial, overdoing it can have detrimental effects. Excessive preheating temperatures can induce undesirable recrystallization processes within the material [82]. The formation of larger recrystallized grains, a consequence of intense preheating, makes the material susceptible to intergranular cracking [79,135]. These grains can then become crack initiation points, especially in regions close to or on the grain boundaries [79,135]. As a result, extremely high preheating temperatures can be counterintuitive and diminish the quality of the product [82].

In the sections above we summarized the challenges in AM of unalloyed W, although most of these problems also exist in AM of W alloys and composites. In brief, these challenges include a high melting point, low laser absorptivity (< 70% for SLM) [114], high thermal conductivity, high melt

 doi:10.20944/preprints202406.1108.v1

viscosity, high oxygen affinity, high DBTT, inherent embrittlement and crack susceptibility. Issues such as formation of cracks, porosities, balling, and deformation leading to compromised mechanical properties are also noted,. Research has primarily focused on optimizing processing parameters to influence outcomes that include defects, densification, grain structures, and properties. For SLM, smaller, spherically shaped W powders were found to have better laser absorptivity [59,62,72]. Parameters like power and volumetric energy density were found to be pivotal for W densification [49,57,60,115]. However, cracking in additively manufactured unalloyed W persists, resulting from thermal stress, challenging crystallization, and W embrittlement and the formation of tungsten oxide, , all of which lead to hot cracking [68]. Crack propagation along grain boundaries is common [40,57,68]. Attempts to mitigate these cracks in AM W have been partially successful. However, unalloyed W has subpar tensile properties (elongation and strength) and limited fracture toughness [68], necessitating alloying for practical applications.

4. Additively Manufactured Tungsten Alloys and Composites

The inherent brittleness and reduced ductility of W is primarily attributed to the high Peierls stress characteristic of the BCC crystal structure, in conjunction with suboptimal grain boundary cohesion. Amongst the strategies to mitigate these challenges discussed in the preceding sections, alloying is a particularly useful approach. Alloying has been shown to impart multifaceted effects on the properties and behavior of W in AM contexts. Several W alloys have been studied in the realm of AM. Since W is often insoluble or immiscible with other elements, its alloyed materials with some elements have been referred to as composites in some studies. In this review we consider all combinations of W with other elements as alloys and refer to combinations of W with ceramic materials (such as carbides and oxides) as composites (Table 7). The AM-fabricated alloy groups that have been studied include W-Re [139–141], W-Ni [94,142], W-Ni-Fe [91,92,95,97,98,101,103,119,143–145], W-Ni-Fe-Co [146], W-Ni-Fe-Cu [98], W-Ni-Cu [28,147], W-Cu [28,30,148–150], W-Cu-Sn [151], W-Ta [32,152–155], W-Ta-Re [156,157], W-Nb [124], W-Fe [93,158], W-Mo [159], and W-Cr [104]. W-based matrix composites with different ceramic phases such as TiC [160,161], ZrC [134], TaC [162], La_2O_3 [63], CeO_2 [63], a mix of La_2O_3 – ZrO_2 – $Y2O_3$ [63], and Y_2O_3 [61,80] have also been fabricated via AM methods.

Table 7. Additively manufactured W-based alloys and W-matrix composites.

Materials	References
W Alloys	
W-1-25%Re	[140,163]
W-0.1-40%Ni	[94,142]
W-7%Ni-3%Fe	[91,92,95,97,98,101,103,119,143,144]
W-4.6%Ni-2.4%Fe	[145]
W-6%Ni-2%Fe-2%Co	[146]
W-12%Ni-4%Fe-4%Co	[146]
W-18%Ni-6%Fe-6%Co	[146]
W- 8.7%(Ni-Fe-Cu)	[98]
W-5%Ni-15%Cu	[27]
W-5%Ni-25%Cu	[147]
W-10%Ni-10%Cu	[147]
W-10%-40%Cu	[28,30,148–150]
W-20%(Cu10Sn)	[151]
W-1-12%Ta	[32,152–155]
W-14.8%Ta-17.2%Re	[156,157]
W-5%Nb	[124]
W-14-79%Fe	[93,158]
W-50%Mo	[159]

 doi:10.20944/preprints202406.1108.v1

W-12.85%Cr	[104]
W Matrix Composites	
W-0.5-2.5%TiC	[160,161]
W-0.5%ZrC	[134]
W-5%TaC	[162]
W-5%La2O3	[63]
W-2%CeO2	[63]
W-1.75%La2O3-0.12%ZrO2-0.12%Y2O3	[63]
Y2O3	[61,80]

A review of the impact of alloying elements and dispersion particles on mitigating the problems associated with AM of W-based materials and on microstructure and mechanical properties (Table 8) shows that alloying elements and ceramic particles are added for the following purposes: lowering melting point of W to enhance densification, modification of laser absorption, reduction of thermal conductivity of W, and reduction of melt viscosity to enhance densification, forming binding phases to enhance densification, improved grain boundary strengthening, modified grain structure, enhanced grain boundary cohesion and better pore distribution to enhance mechanical properties and to mitigate microcracking, strengthening through secondary dispersed or precipitated phases to restrict grain boundary movement and enhance mechanical properties to mitigate microcracking and enhance low temperature ductility, increasing stacking fault energy, boosting dislocation mobility to improve ductility and lower DBTT, and for other purposes such as self passivating behavior, reduction of fuzz formation in nuclear application.

In the subsequent sections, we will closely examine some of these alloying strategies.

Table 8. An overview of the impact of alloying elements and dispersion particles on mitigating the challenges of AM of W-based materials and on microstructure and mechanical properties.

Effects on W in AM	**Alloying Element(s)**	**Specifics/Notes**	**Ref**
Enhanced Densification	Ni, Fe, Co, Mo, Re, Ta, etc.	Due to lower melting points of alloying phases promote densification. For SLM, the melting of Ni, Fe and Co enhances dissolution of W particles.	[38,60, 94,104, 142,146–150]
	Cu	Due to role of alloying elements in forming binding phases. Good wetting allows the molten copper (Cu) to spread and adheres strongly to the W particles. Surface smoothing also contribute to a denser final structure	[28,30]
	Ni, Cu, Ta, Fe, Mo	Modifications in laser absorption, melt viscosity, and fluidity. Ni works better than Cu. Ta Increases recrystallization temperature and decreases thermal conductivity. Ni, and Fe for improved wettability of W.	[28,30, 32,94,142,147–150,152–155]

 doi:10.20944/preprints202406.1108.v1

Microcrack Mitigation	Re, Ta, Nb, Mo, Cr, Ti , Ir	Re lowers the DBTT of tungsten alloys, significantly reduce their tendency to crack during AM processes. Ta forms a special cellular structure that keeps tiny air pockets (nanopores) separated from each other. This reduces the overall tendency of the material to crack. Ta also oxidizes more easily than tungsten (W) during the printing process. As a result, fewer nanopores form in the final tungsten alloy, and the risk of microcracks is reduced. Nb improves the intergranular bonding of the alloy via solid solution strengthening. Adding certain elements (alloying) to tungsten can be a powerful tool to prevent the formation of tiny cracks (microcracks) during 3D printing. Tungsten's high melting point presents a challenge. It solidifies first, causing stress within the material. Alloying elements help to lessen this stress by essentially acting as a buffer. Grain refinement of W, Improved grain boundary strengthening, modified grain structure, better pore distribution. Cr forms Cr-rich Cr-W phase and causes grain refinement. Ti (in conventional manufacturing of W) gives rise to a heterogeneous chemical distribution to prevent nanostructured microstructure from coarsening Ir (in conventional manufacturing of W) strengthens grain boundary cohesion, optimizes dislocation mobility, and reduce cracking.	[28,63,67,104,124,139–141,153–156,164,165]
	Re	Enhancement of grain boundary cohesion Boosting dislocation mobility and lowering DBTT, reducing embrittlement W when alloyed with rhenium (Re) showcases a reduced DBTT and increased low-temperature ductility. This improvement is attributed to rhenium's high solubility in tungsten and its capability as a solution hardener	[139–141]
	TiC, ZrC, TaC, Y2O3, La2O3, etc.	Y2O3 Oxide leads to more low-angle grain boundaries (LAGBs) and reduces cracking. W–Y2O3 has 3.6 μm grain size and better low-temperature ductility and supress cracking. the integration of lanthanum oxide (La_2O_3) not only bolsters radiation resistance but also provides an indirect solution to these interstitial contamination challenges. Incorporating ZrC nanoparticles decreases crack density due to finer grains and increased grain-boundary length. ZrC also captures oxygen to form ZrO_y, reducing embrittlement. TaC supports the formation of W_2C phases within the material, further increase the overall strength and crack resistance.	[61,66,134,153,162]

 doi:10.20944/preprints202406.1108.v1

		TaC reacts with any oxygen present, forming TaO_x, effectively removing oxygen from the system. TiC enhances hardness.	
Mechanical Properties Adjustments	Fe	Strengthening by formation of secondary or precipitated phases during AM. The non-equilibrium solidification between Fe and W allows for the potential formation of intermetallic phases like Fe7W6 and Fe2W, improving the hardness.	[93,156,158]
	Ni	Tensile strength and fracture toughness enhancement	[94,142]
	Ti, Ir, Hf (if used in AM)	Increase recrystallization temperatures. As potent carbide formers mitigate the adverse effects of carbon impurities on the alloy's mechanics, Elevate the recrystallization temperatures and improve W's low temperature ductility and high temperature strength. Ir can improve mechanical properties by increasing grain boundary cohesion.	[164–168]
	Ta, Nb, and other group V and IV transition metals	Improvement of Intrinsic ductility of W alloys Ta can increase hardness. Solid solution strengthening by Nb	[124,153–156]
Others	Ta	Fuzz Formation Reduction: fuzz reduction during He plasma irradiation; suitable for nuclear applications.	[152]
	Cr-Y	Self-passivation behavior for high-temperature applications	[169]

4.1. Alloying for Enhanced Densification

The incorporation of alloying elements into W during AM profoundly impacts the resultant material properties. Alloying with metals that have lower melting points is a strategy to decrease the overall melting point of the refractory alloy. But it is important for this to be done in moderation to ensure that the intrinsic high-temperature properties of the W alloys are retained [38,60]. Tungsten alloys behave differently when melted compared to pure W. The alloying elements can form phases with lower melting points than pure W, aiding in the binding and dissolution of W particles [28]. These elements can also affect melt viscosity and fluidity during AM, especially in LPBF-SLM. Alloying elements can lead to unique solidification behaviors, leading to improved grain structures, and reduced stresses, among other benefits. Overall, W alloys generally exhibit superior AM part quality compared to the use of pure W [79,80]. A major consequence observed is the enhanced densification of the W matrix. Most alloying elements, including Ni, Fe, Co, Cu, and Re contribute to this phenomenon. The basis for this enhanced densification is the lower melting points of these alloying elements compared to W and the possibility of melting at lower energy inputs and faster scan rates. In the context of the SLM technique, the melting of Ni, Fe, and Co has been noted to expedite the dissolution of W particles [146,147], leading to a more consolidated alloy [30,142,146,147]. Cu, as an alloying element, has been studied [28,30,148–150] to reveal its distinct role in W densification during AM. The significance of Cu lies in its ability to form binding phases with W. The molten state of Cu ensures effective wetting of W particles, while W particles concurrently undergo surface smoothing. Both these effects foster increased densification of the W-Cu composite during laser-based AM processes [28].

The alloying elements Ni, Cu, and Ta introduce significant changes in the AM process by altering parameters such as laser absorption, melt viscosity, and fluidity [28,30,32,94,142,147–150,152–155]. Of

 doi:10.20944/preprints202406.1108.v1

these alloying elements, Ni demonstrates superior efficacy over Cu in such modifications, primarily due to its lower thermal conductivity [61]. The use of Ta comes with its own benefits, including the elevation of the recrystallization temperature and a decrement in thermal conductivity [28,142]. Rhenium (Re) plays a multifaceted role in the AM of W alloys, one of which is its contribution to densification. The addition of Re allows for parts with higher relative density to be achieved (relative to pure W) (Figure 15a) [139]. A higher relative density in Re-alloyed W is obtainable. Obtaining a relative density of more than 95% in SLM-fabricated unalloyed W is usually difficult, but precise scanning parameter adjustments, preheating, and the use of optimized starting materials has resulted in achieving relative densities over 98%. The EBM technique for unalloyed W fabrication has been shown to achieve relative densities up to 99.5%. Addition of alloying elements such as Cu, Ni, Fe, Mo, and Cr can facilitate higher densification in AM W materials (Figure 15b).

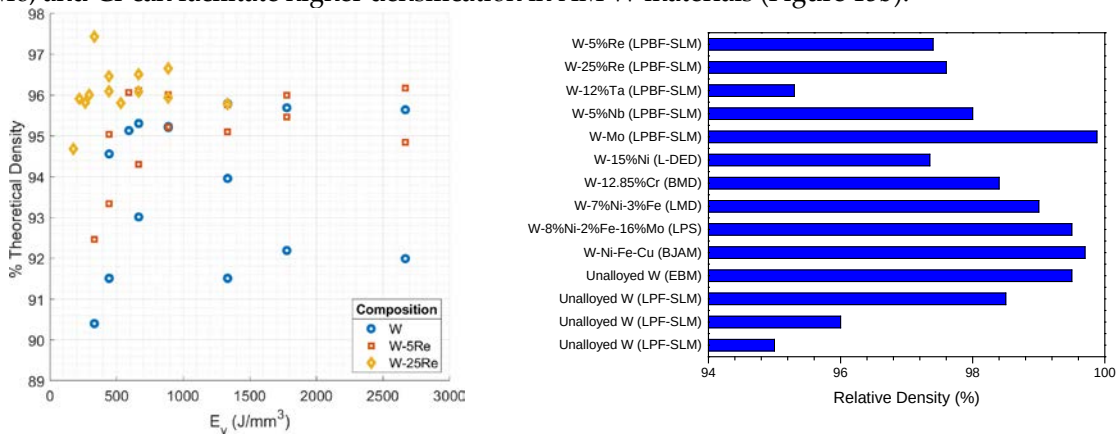

(**a**) (**b**)

Figure 15. a) Achieved relative (% of theoretical) for SLM-manufactured W-5%Re , W-25%Re alloys and unalloyed W versus energy density [139], b) obtained relative density of alloyed and unalloyed W fabricated via different AM techniques.

4.2. Alloying and Ceramic Dispersions for Microcrack Mitigation

4.2.1. Alloying Elements

Alloying is a very useful strategy for reducing interstitial contamination. The introduction of specific alloying elements in W during AM has been shown to substantially impact the microcrack mitigation process, an effect achieved through mechanisms such as grain structure modification, improved pore distribution, grain boundary strengthening, stress reduction, decreased DBTT, and reduced nanopore formation. The addition of Ta induces a cellular structure that spreads the nanopore distribution, culminating in an 80% reduction in cracking [67,155] (Figure 16). Furthermore, the role of Ta in reducing oxygen sensitivity during solidification, courtesy of its in-situ oxidation, is pivotal in alleviating microcracks in the W alloy [67,153–155].

 doi:10.20944/preprints202406.1108.v1

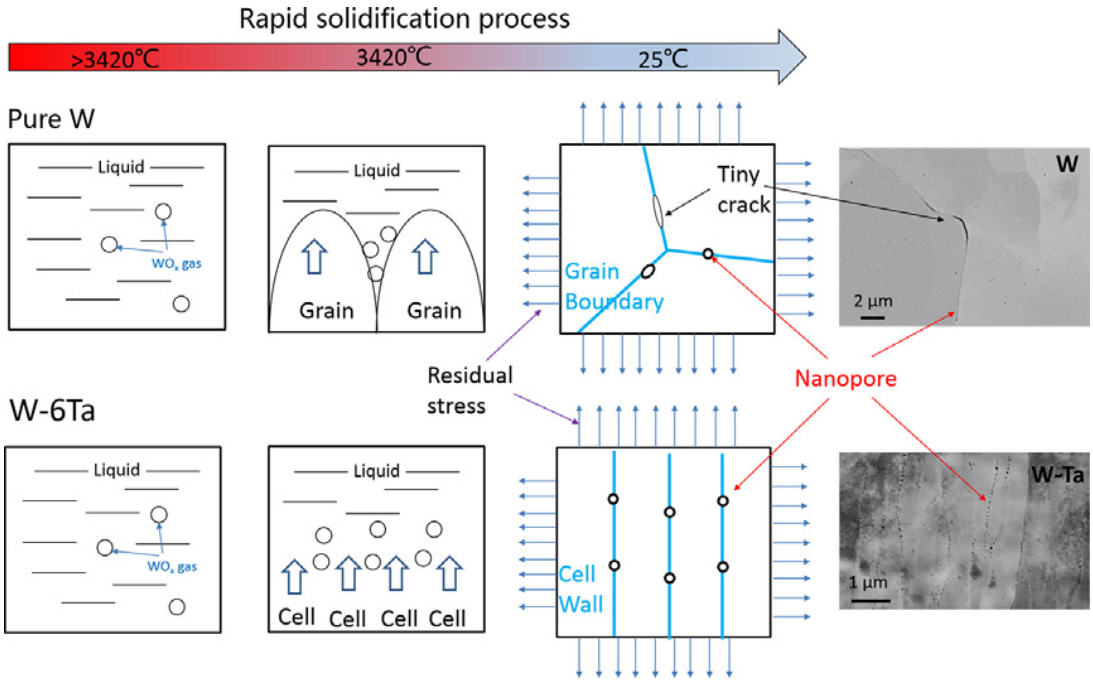

Figure 16. Schematic illustration of how the adding of Tantalum (Ta) influence the formation of nanopores during the additive manufacturing of Tungsten (W) and W-Ta alloys [67].

Niobium (Nb) can be beneficial as an alloying element due to solid solution strengthening, which strengthens intergranular bonding to provide an effective countermeasure against microcracking [124]. Alloying W with Re offers promising outcomes. Apart from its contribution in enhancing densification, the resultant alloys show enhanced grain boundary cohesion and an increased mobility of screw dislocations, significantly altering their mechanical behaviors. The addition of Re significantly reduces the ease at which W alloy cracks during the manufacturing process due to the significant lowering of the DBTT facilitated by Re [139–141]. Eckley et al. [139] used EBSD maps and optical microscopy images to show significant cracking in pure W parts (Figure 17). Cracking increased with density and followed scan tracks, branching at 45-degree angles, and longitudinal cracking traced columnar grain boundaries in the build direction (Figure 17a,b). The introduction of 5 wt.% Re failed to effectively mitigate the observed cracking (Figure 17c,d). However, an increase in Re content to 25 wt.% resulted in a significant reduction in both surface and longitudinal cracking, and the characteristic horizontal and 45-degree angle cracking behaviors were notably minimized (Figure 17e,f). This improvement can be attributed to the lowered DBTT of W due to rhenium alloying, decreasing brittleness during cooling. Despite these enhancements, some cracking persisted. This study shows rhenium alloying to be effective in enhancing the crack resistance of printed W materials, offering valuable insights into its practical applications in AM processes. Notably, conventional fabrication has demonstrated the profound influence of rhenium, with W alloys containing 26 wt% Re exhibiting a DBTT as low as -101°C [79,167,168].

 doi:10.20944/preprints202406.1108.v1

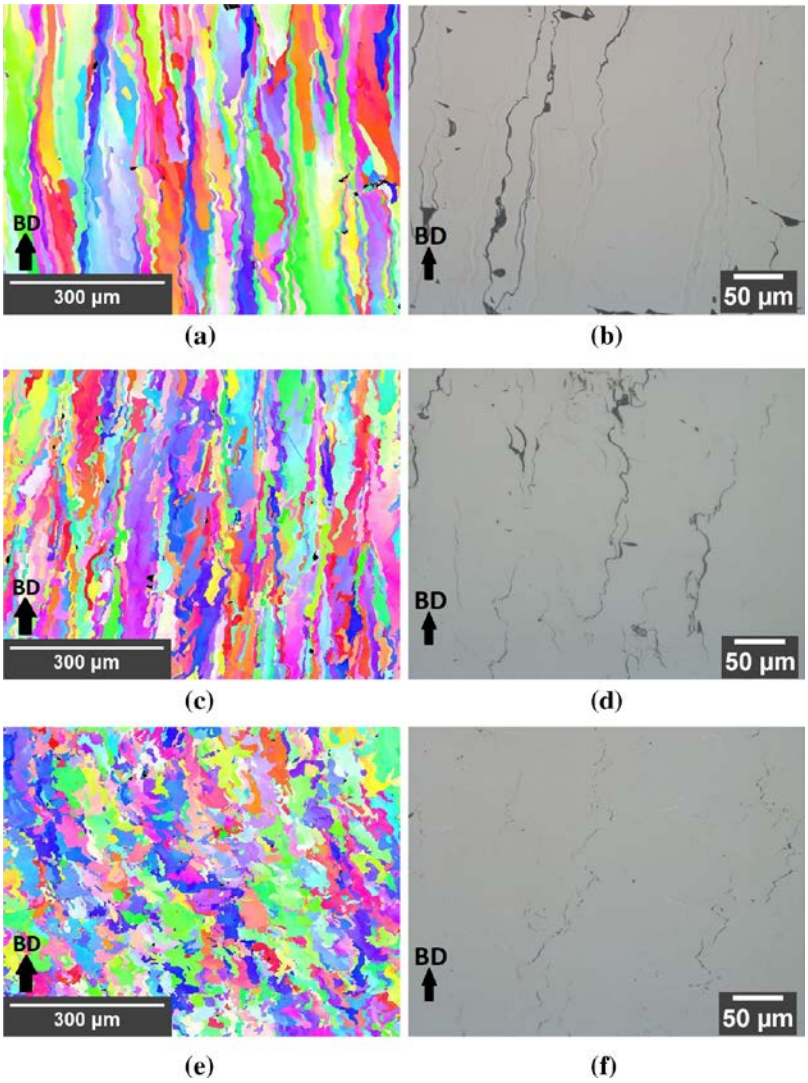

Figure 17. EBSD maps and optical microscopy images depicting the microstructure of tungsten cubes made using Selective Laser Melting (SLM) with different Rhenium (Re) content. a) & b) Pure Tungsten (W) cube, c) & d) Tungsten with 5% Rhenium (W-5%Re) cube and e) & f) Tungsten with 25% Rhenium (W-25%Re) cube. The laser power, hatch spacing, and scan speed were all kept constant at 200 W, 50 µm, and 400 mm/s, respectively. The build direction is also indicated in the image [139].

Additionally, the inherent characteristics of alloying elements relieve stress by compensating for the shrinkage experienced as W solidifies (a direct consequence of its elevated melting point). This phenomenon plays a direct role in minimizing microcracking [124]. Further contributions from chromium (Cr) result in grain refinement, indirectly aiding in crack mitigation. Cr induces a Cr-rich Cr-W phase to optimize grain refinement [104]. In conventional fabrication techniques of W-based alloys, adding Ti as an alloying element creates a heterogeneous chemical distribution, stalling the coarsening of nanostructured microstructures [164], whereas adding Ir strengthens grain boundary cohesion, optimizes dislocation mobility, and subsequently deters crack formation [165]. These alloying additions (Ti and Ir) may be beneficial in materials design for AM.

4.2.2. Ceramic Dispersions (W Composites)

Incorporating ceramic particles in W has been shown to enhance composite resistance to cracking. Tungsten's challenges with oxide retention and the power balling effect are clear indicators of oxidation difficulties, but solutions are on hand. The integration of lanthanum oxide (La_2O_3) not only bolsters radiation resistance but also provides an indirect solution to the problem of interstitial contamination. Innovations like nanopore segregation have been introduced, inducing, and

 doi:10.20944/preprints202406.1108.v1

identifying crack initiation. Achieving a high theoretical density range of 96-98.5%, combined with optimal conditions characterized by elevated laser energy density and low oxygen levels represents meaningful advancements in countering these challenges.

W-Y_2O_3 composites offer a refined grain size and commendable low-temperature ductility [61]. Based on EBSD grain size, and grain misorientation distributions studies of in W-Y_2O_3 composites, the use of nano-sized Y_2O_3 particles lead to grain refinement and a greater occurrence of low-angle grain boundaries (LAGBs). The concomitant reduction of high-angle grain boundaries (which are more susceptible to cracking) markedly reduces cracking in the resulting W composites, (Figure 18) [61]. Introducing micron-sized Y_2O_3 dispersions into W does not lead to grain refinement, although this increases the fraction of LAGBs (Figure 18 c,d). However, when nano-sized Y_2O_3 dispersions are used in the composite, the LAGB fraction and grain size are both reduced (Figure 18, e,f).

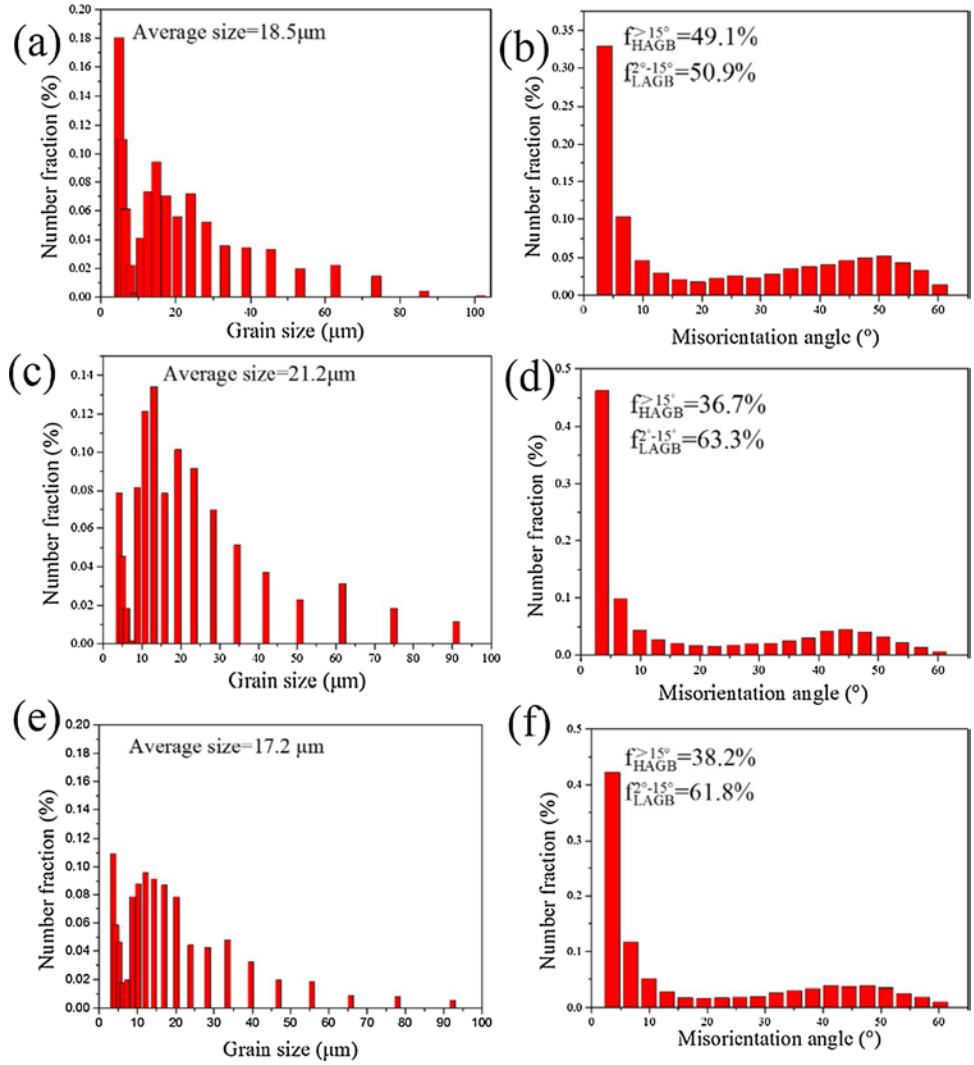

Figure 18. EBSD grain size distribution for (a) pure W, (c) W-Y_2O_3 (Micron-sized), and (e) W-Y_2O_3 (Nano-sized). Grain misorientation angle distribution for (b) pure W, (d) W- Y_2O_3 (Micron-sized), and (e) W-Y_2O_3 (Nano-sized) [61].

Li et al.'s study identified zirconium carbide (ZrC) as a crucial ceramic particle. They showed that W-ZrC samples showed a remarkable reduction in crack density compared to pure W. Their SEM images reinforced this, showing fewer and more dispersed cracks in W-ZrC, (Fig, 19 a,b). The images also reveal that while pure W had long and densely distributed cracks, W-ZrC had shorter and sparser cracks (Figure 19c,d). This improved crack resistance is attributed to secondary-phase nanoparticles in W-ZrC, which refined the grain structure and captured oxygen impurities to hinder crack propagation [134]. Achieving a fully uniform grain structure would require further efforts to

 doi:10.20944/preprints202406.1108.v1

ensure even ZrC distribution. Li et al.'s study highlighted ZrC's role in reducing crack density, promoting finer grains, and extending grain boundaries. Their bright field TEM, HRTEM (high-resolution transmission electron microscopy), and high angle annular dark field images (Figures 20a, b, c) along with EDS chemical maps (Figures 20d, e, g, h) at various magnifications, and the SAEDP (selected area electron diffraction pattern) of selected nanoparticles (Figure 20f) provide compelling evidence of ZrC's capacity to capture and bind oxygen to form ZrO_y particles. This mechanism is a highly effective means of mitigating embrittlement [79,134].

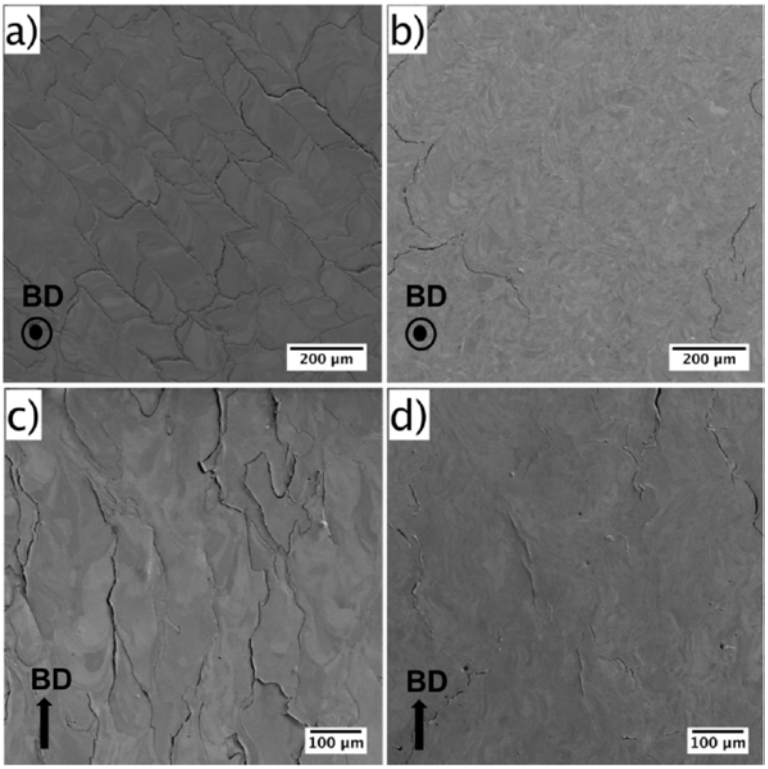

Figure 19. SEM image showing a) & c) the top and side surface of Pure Tungsten (W) cube, b) & d) top and side surface of W-ZrC cube. The build direction is also indicated in the image [134].

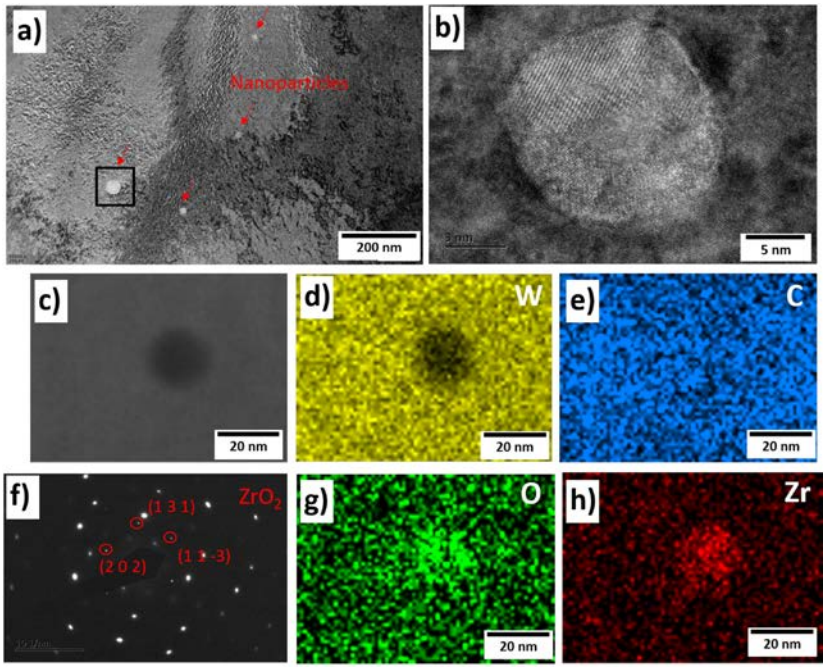

 doi:10.20944/preprints202406.1108.v1

Figure 20. Analysis of the nanoparticles. (a) Distribution of nanoparticles and (b) the HRTEM of the selected nanoparticle. (c) High Angle Annular Dark Field (HAADF) image, (d, e, g & h) its EDS elemental maps, and (f) the SAEDP of the selected nanoparticle [134].

Tantalum carbide (TaC) particles in W also play an important role in crack mitigation. This is achieved via the dual action of initiating in-situ W_2C phase formations and promoting oxygen consumption through TaO_x formation, which collectively suppress cracks [153,162]. Titanium carbide (TiC), while predominantly increasing hardness, may indirectly improve crack resistance due to the improved mechanical properties of the composite [61,66,153,162]. HfC dispersion in conventionally fabricated W alloys has conferred excellent thermal stability and tensile properties of the composite [166,167]. This can be useful features to have for materials design in AM of W as well.

4.3. Alloying and Ceramic Dispersions for Adjustments to Mechanical Properties

Besides mitigating the problems discussed above, alloying confers additional benefits. Fe integration in W alloys during AM strengthens the resulting material due to the formation of secondary or precipitated phases. This is due to the possible peritectic reaction between Fe and W during non-equilibrium solidification, leading to the emergence of intermetallic phases such as Fe_7W_6 and Fe_2W. This formation significantly increases the hardness of the W–Fe alloy [79,93,158].

Ni addition enhances the alloy's tensile strength and fracture toughness [94,142]. Nb provides solid solution strengthening and similarly improves the mechanical properties of the alloy [124]. Inclusion of Ta and other group V and IV transition metals improves the intrinsic ductility of W alloys. In particular, Ta not only enhances ductility but also increases the hardness of the alloy [153–156].

Incorporation of titanium (Ti), iridium (Ir), and hafnium (Hf) in conventionally fabricated W alloys achieves multiple objectives as they influence the mechanical properties in different ways. They increase recrystallization temperatures and, as potent carbide formers, mitigate the adverse effects of carbon impurities on the alloy's mechanics, elevate the recrystallization temperatures and improve W's low temperature ductility and high-temperature strength [164–168].

Since unalloyed W exhibits limited plasticity, studies have predominantly focused on reporting compression test results. Conversely, a wealth of tensile test results is available for W alloys processed using AM (Figure 21). The strength and elongation of W alloys vary depending on compositions (Figure 21a,b).Wang et al. [94] reported a W–15%Ni alloy with a UTS of 560 MPa and 3.75% elongation, while W–7%Ni–3%Fe made by LMD showed a UTS of 1037 MPa and 3.5% elongation [91], and W–4.6%Ni–2.4%Fe fabricated via powder extrusion 3D printing and sintering showed a UTS of 1040 MPa and remarkably high (20.7%) elongation (Figure 21a,b) [145]. Ultrashort-time laser LPS processing for W heavy alloy resulted in a UTS of 1374 MPa, and 8.5% elongation (Figure 21,a,b) [103].

Alloying elements play a pivotal role in enhancing the tensile properties of W, notably its elongation, which is otherwise limited or non-existent in unalloyed W.

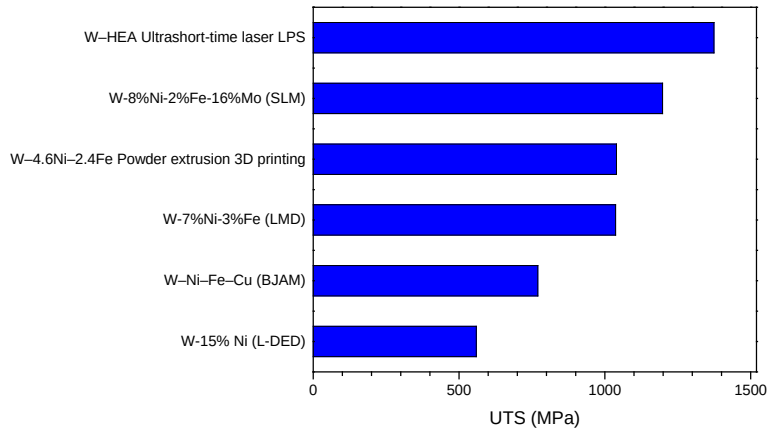

 doi:10.20944/preprints202406.1108.v1

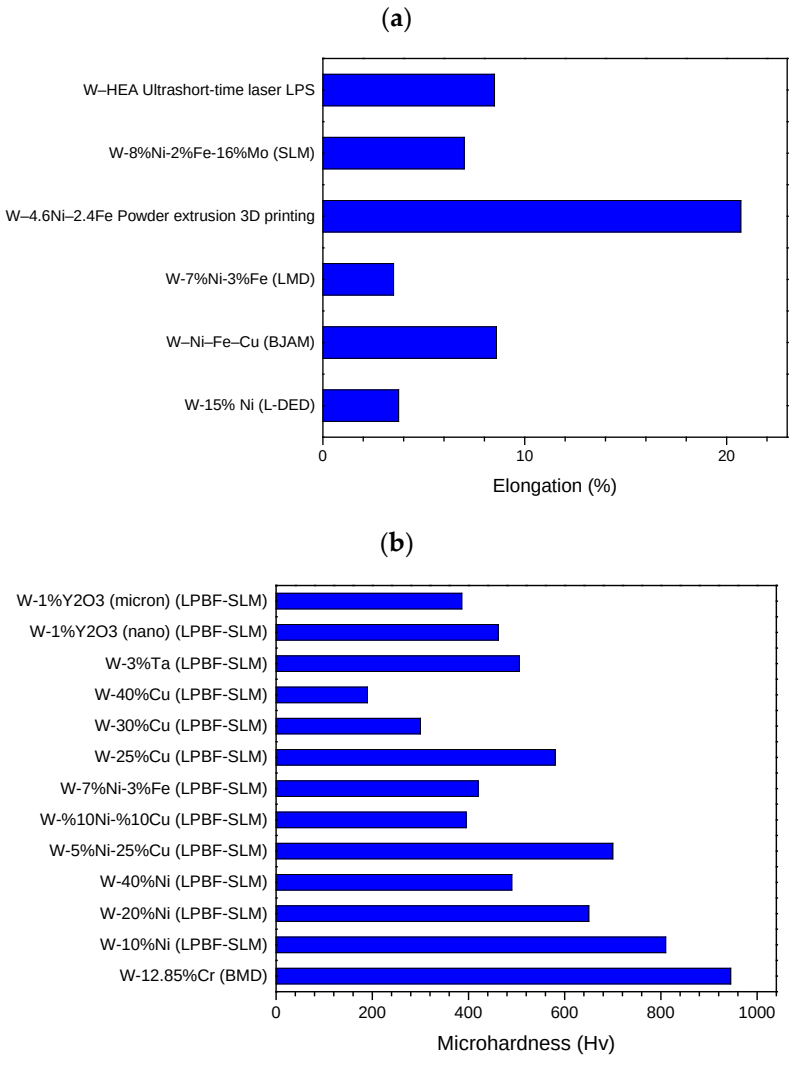

Figure 21. Mechanical properties of select AM W alloys: a) UTS (MPa), b) Elongation (%), and c) Microhardness (Hv).

In AM for W-based materials, the alteration of mechanical properties that include microhardness (Figure 21c) has been a focal point for investigation. Li et al. [157] examined the variation in Vickers microhardness due to VED in the context of W-3%Ta alloy. Operating at a substrate preheating temperature of 150°C and a 67°-layer angle, they reported a range of microhardness values from 493.8 to 535.6 Hv. This range correlated with VED values spanning 192 to 1000 J/mm³, with an average microhardness of 505.7 Hv. Intriguingly, an upward trend in relative density was concurrently observed as VED values increased. Conversely, Bose et al. [104] reported the highest microhardness achievement of 966 Hv for a W-Cr component produced through binder jetting and sintered at 1500°C for 1 hour, demonstrating a striking contrast to the above trends.

Zhang et al. [142] and Yan et al. [148] showed a contrasting narrative, showcasing a decline in hardness with an incremental influx of nickel in W-Ni and W-Ni-Cu systems. In a related study, Zhang et al. [142] highlighted a gradient of hardness reduction with distance from the base of LPBF-SLM-fabricated samples, plummeting from 810 to 300 Hv for W-10%Ni and from 490 to 250 Hv for W-40Ni.

Ivekovic et al. [144] noted a decline in hardness post-heat treatment of L-PBF-fabricated W-7Ni-3Fe samples, which diverged from the augmentation in hardness expected. Conversely, Wang et al. [147] demonstrated an intriguing phenomenon in W-Ni-Cu alloy, where an escalation in microhardness, ranging from 360 to 395 Hv, was linked to increasing VED. This phenomenon is

 doi:10.20944/preprints202406.1108.v1

attributed to the formation of finer grain sizes owing to elevated melt pool temperatures. Moreover, Hu et al. [61] brought nano structural considerations into the equation, underscoring the influence of grain size. They documented an upswing in hardness with the decreasing grain size of Y_2O_3 particles, transitioning from micro- to nano-scale dimensions.

These findings underscore the fact that enhanced and/or adjusted mechanical properties are achievable through alloying in AM of for W-based materials.

4.4. Alloying for Other Specific Purposes

The addition of Ta to W alloys is pivotal for reducing fuzz formation. Ta has demonstrated its capability to reduce fuzz during He plasma irradiation, making these alloys suitable for nuclear applications [152]. Furthermore, W alloys formulated with the Cr-Y combination exhibit self-passivation behavior in conventional fabrication. This intrinsic property makes W alloys integrated with Cr-Y especially useful in high-temperature applications [79,169].

5. Future Directions

Although the AM of W holds great promise for producing high-performance parts, its widespread adoption has been curtailed by problems associated with the inherent material properties of W and printability challenges. We must strategically prioritize research efforts into the AM of W through developing meticulous processes, as well as microstructural and material design. We believe in the possibilities of bringing W AM into a new era of precision, sustainability, and widespread applicability through advancements in atomic-level understanding and thermodynamic modeling, as well as through harnessing the power of data analytics, composite design, and sustainable manufacturing.

1. **Atomic-Level Understanding: The Key to Tailored Properties**

Further studies are needed for understanding W at the atomic level, focusing on the local atomic structure and short-range order chemistry. Improving our understanding of the inherent atomic arrangement in W at the microscopic perspective will enable us to unlock new possibilities for tailored material properties and optimized performance.

2. **Thermodynamic Modeling: A Roadmap for Alloy Design**

Integrating thermodynamic calculation of phase diagrams (CALPHAD) modeling into alloy design will play a pivotal role in predicting phase equilibria and allow researchers to design W alloys with improved control over composition and phase transitions. This thermodynamic approach ensures a systematic exploration of the uncharted alloy space, allowing materials with tailored properties to be developed.

3. **Harnessing the Power of Data Analytics: Machine Learning and In-situ Monitoring**

Data analytics has emerged as a key tool for extracting meaningful insights from complex datasets generated during the AM process. Researchers can leverage machine learning and statistical techniques to identify patterns, and correlations which can help in the optimization of processing parameters. Further studies can also develop and implement advanced in-situ process monitoring techniques during AM. The data generated during the real-time monitoring of temperature, microstructure evolution, and defect formation will provide valuable insights, enabling adaptive control strategies to enhance the quality and repeatability of W components.

4. **Composite Design: Improved Innovative Composite**

Improvements in the AM of tungsten will allow increased exploration of innovative composite formulations. Researchers can seek to synergize W with other advanced materials, such as polymers and ceramics, to create composites that exhibit superior mechanical, thermal, and chemical properties. This approach opens avenues for tailoring W composites for specific applications across diverse industries.

5. **Sustainable Manufacturing: Hidden Cost of Oxidation of W**

 doi:10.20944/preprints202406.1108.v1

While the high oxygen affinity of W has been discussed above in the context of hot cracking, its influence extends beyond the printed part. The high temperatures and heating profiles employed during the AM process can lead to inadvertent oxidation of adjacent powder beds. This oxidation significantly affects the reusability of the powder, potentially increasing waste and negating the environmental benefits of AM. Future research efforts should prioritize mitigating this hidden environmental cost by optimizing processing parameters to minimize the impact of oxidation and maximize powder reusability.

This review highlighted advanced materials design approaches that will revolutionize W AM. By embracing a combination of multipronged approaches, we can construct a transformative pathway towards the development and manufacturing of next-generation W materials with unprecedented properties and functionalities. The widespread adoption of these materials across diverse industries will bode well for the future.

Acknowledgments: The Authors acknowledge financial support from Zhejiang Province (Fund Number: 2023C01SA393195), and Wenzhou City (Fund Number: ZG2023036) to Wenzhou Hongfeng Electrical Alloy Co Ltd. Y.X. Tong gratefully acknowledges the support of National Key R&D Program of China [grant number: 2022YFB4602402].

References

1. M. Mani: J. Madan, J.H. Lee, K.W. Lyons, S.K. Gupta, Sustainability characterisation for manufacturing processes, Int J Prod Res 52 (2014) 5895–5912. https://doi.org/10.1080/00207543.2014.886788.
2. L. Valivullah, M. Mani, K.W. Lyons, S.K. Gupta, Manufacturing Process Information Models for Sustainable Manufacturing, in: Volume 1: Materials; Micro and Nano Technologies; Properties, Applications and Systems; Sustainable Manufacturing, American Society of Mechanical Engineers, 2014. https://doi.org/10.1115/MSEC2014-4105.
3. M. Mani, K.W. Lyons, S.K. Gupta, Sustainability Characterization for Additive Manufacturing, J Res Natl Inst Stand Technol 119 (2014) 419. https://doi.org/10.6028/jres.119.016.
4. P. Moghimian, T. Poirié, M. Habibnejad-Korayem, J.A. Zavala, J. Kroeger, F. Marion, F. Larouche, Metal powders in additive manufacturing: A review on reusability and recyclability of common titanium, nickel and aluminum alloys, Addit Manuf 43 (2021) 102017. https://doi.org/10.1016/j.addma.2021.102017.
5. O. Mireles, O. Rodriguez, Y. Gao, N. Philips, Additive Manufacture of Refractory Alloy C103 for Propulsion Applications, in: AIAA Propulsion and Energy 2020 Forum, American Institute of Aeronautics and Astronautics, Reston, Virginia, 2020. https://doi.org/10.2514/6.2020-3500.
6. A. Zadpoor, Current Trends in Metallic Orthopedic Biomaterials: From Additive Manufacturing to Bio-Functionalization, Infection Prevention, and Beyond, Int J Mol Sci 19 (2018) 2684. https://doi.org/10.3390/ijms19092684.
7. N. Li, S. Huang, G. Zhang, R. Qin, W. Liu, H. Xiong, G. Shi, J. Blackburn, Progress in additive manufacturing on new materials: A review, J Mater Sci Technol 35 (2019) 242–269. https://doi.org/10.1016/j.jmst.2018.09.002.
8. K. Cho, H. Odo, K. Okamoto, H.Y. Yasuda, H. Nakashima, M. Takeyama, T. Nakano, Improving the Tensile Properties of Additively Manufactured β-Containing TiAl Alloys via Microstructure Control Focusing on Cellular Precipitation Reaction, Crystals (Basel) 11 (2021) 809. https://doi.org/10.3390/cryst11070809.
9. M. Reith, M. Franke, C. Körner, Robust γ-TiAl Dual Microstructure Concept by Advanced Electron Beam Powder Bed Fusion Technology, Crystals (Basel) 13 (2023) 1348. https://doi.org/10.3390/cryst13091348.
10. R. Zhang, F. Jiang, L. Xue, J. Yu, Review of Additive Manufacturing Techniques for Large-Scale Metal Functionally Graded Materials, Crystals (Basel) 12 (2022) 858. https://doi.org/10.3390/cryst12060858.
11. I. Noh, J. Jeon, S.W. Lee, A Study on Metallographic and Machining Characteristics of Functionally Graded Material Produced by Directed Energy Deposition, Crystals (Basel) 13 (2023) 1491. https://doi.org/10.3390/cryst13101491.
12. M.P. Behera, T. Dougherty, S. Singamneni, Conventional and Additive Manufacturing with Metal Matrix Composites: A Perspective, Procedia Manuf 30 (2019) 159–166. https://doi.org/10.1016/j.promfg.2019.02.023.
13. S. Tang, R. Ummethala, C. Suryanarayana, J. Eckert, K.G. Prashanth, Z. Wang, Additive Manufacturing of Aluminum-Based Metal Matrix Composites—A Review, Adv Eng Mater 23 (2021). https://doi.org/10.1002/adem.202100053.
14. J. Shi, Y. Wang, Development of metal matrix composites by laser-assisted additive manufacturing technologies: a review, J Mater Sci 55 (2020) 9883–9917. https://doi.org/10.1007/s10853-020-04730-3.
15. Y. Hu, W. Cong, A review on laser deposition-additive manufacturing of ceramics and ceramic reinforced metal matrix composites, Ceram Int 44 (2018) 20599–20612. https://doi.org/10.1016/j.ceramint.2018.08.083.

 doi:10.20944/preprints202406.1108.v1

16. L. Jannesari Ladani, Applications of artificial intelligence and machine learning in metal additive manufacturing, Journal of Physics: Materials 4 (2021) 042009. https://doi.org/10.1088/2515-7639/ac2791.
17. L. Meng, B. McWilliams, W. Jarosinski, H.-Y. Park, Y.-G. Jung, J. Lee, J. Zhang, Machine Learning in Additive Manufacturing: A Review, JOM 72 (2020) 2363–2377. https://doi.org/10.1007/s11837-020-04155-y.
18. H. Ko, P. Witherell, Y. Lu, S. Kim, D.W. Rosen, Machine learning and knowledge graph based design rule construction for additive manufacturing, Addit Manuf 37 (2021) 101620. https://doi.org/10.1016/j.addma.2020.101620.
19. J. Elambasseril, M. Brandt, Artificial intelligence: way forward to empower metal additive manufacturing product development – an overview, Mater Today Proc 58 (2022) 461–465. https://doi.org/10.1016/j.matpr.2022.02.485.
20. C. Liu, W. Tian, C. Kan, When AI meets additive manufacturing: Challenges and emerging opportunities for human-centered products development, J Manuf Syst 64 (2022) 648–656. https://doi.org/10.1016/j.jmsy.2022.04.010.
21. B. Naghshineh, A. Ribeiro, C. Jacinto, H. Carvalho, Social impacts of additive manufacturing: A stakeholder-driven framework, Technol Forecast Soc Change 164 (2021) 120368. https://doi.org/10.1016/j.techfore.2020.120368.
22. F. Matos, C. Jacinto, Additive manufacturing technology: mapping social impacts, Journal of Manufacturing Technology Management 30 (2019) 70–97. https://doi.org/10.1108/JMTM-12-2017-0263.
23. D. Landi, F.C. Zefinetti, C. Spreafico, D. Regazzoni, Comparative life cycle assessment of two different manufacturing technologies: laser additive manufacturing and traditional technique, Procedia CIRP 105 (2022) 700–705. https://doi.org/10.1016/j.procir.2022.02.117.
24. G. Felice, F. Lamperti, L. Piscitello, The employment implications of additive manufacturing, Ind Innov 29 (2022) 333–366. https://doi.org/10.1080/13662716.2021.1967730.
25. M. Rieth, S.L. Dudarev, S.M. Gonzalez de Vicente, J. Aktaa, T. Ahlgren, S. Antusch, D.E.J. Armstrong, M. Balden, N. Baluc, M.-F. Barthe, W.W. Basuki, M. Battabyal, C.S. Becquart, D. Blagoeva, H. Boldyryeva, J. Brinkmann, M. Celino, L. Ciupinski, J.B. Correia, A. De Backer, C. Domain, E. Gaganidze, C. García-Rosales, J. Gibson, M.R. Gilbert, S. Giusepponi, B. Gludovatz, H. Greuner, K. Heinola, T. Höschen, A. Hoffmann, N. Holstein, F. Koch, W. Krauss, H. Li, S. Lindig, J. Linke, Ch. Linsmeier, P. López-Ruiz, H. Maier, J. Matejicek, T.P. Mishra, M. Muhammed, A. Muñoz, M. Muzyk, K. Nordlund, D. Nguyen-Manh, J. Opschoor, N. Ordás, T. Palacios, G. Pintsuk, R. Pippan, J. Reiser, J. Riesch, S.G. Roberts, L. Romaner, M. Rosiński, M. Sanchez, W. Schulmeyer, H. Traxler, A. Ureña, J.G. van der Laan, L. Veleva, S. Wahlberg, M. Walter, T. Weber, T. Weitkamp, S. Wurster, M.A. Yar, J.H. You, A. Zivelonghi, Recent progress in research on tungsten materials for nuclear fusion applications in Europe, Journal of Nuclear Materials 432 (2013) 482–500. https://doi.org/10.1016/j.jnucmat.2012.08.018.
26. J. Xie, H. Lu, J. Lu, X. Song, S. Wu, J. Lei, Additive manufacturing of tungsten using directed energy deposition for potential nuclear fusion application, Surf Coat Technol 409 (2021) 126884. https://doi.org/10.1016/j.surfcoat.2021.126884.
27. Y. Katoh, L.L. Snead, L.M. Garrison, X. Hu, T. Koyanagi, C.M. Parish, P.D. Edmondson, M. Fukuda, T. Hwang, T. Tanaka, A. Hasegawa, Response of unalloyed tungsten to mixed spectrum neutrons, Journal of Nuclear Materials 520 (2019) 193–207. https://doi.org/10.1016/j.jnucmat.2019.03.045.
28. G. Wang, Y. Qin, S. Yang, Influence of Ni additions on the microstructure and tensile property of W-Cu composites produced by direct energy deposition, J Alloys Compd 899 (2022) 163272. https://doi.org/10.1016/j.jallcom.2021.163272.
29. A.M. Engwall, S.J. Shin, J. Bae, Y.M. Wang, Enhanced properties of tungsten films by high-power impulse magnetron sputtering, Surf Coat Technol 363 (2019) 191–197. https://doi.org/10.1016/j.surfcoat.2019.02.055.
30. S. Su, Y. Lu, Densified W Cu composite fabricated via laser additive manufacturing, Int J Refract Metals Hard Mater 87 (2020) 105122. https://doi.org/10.1016/j.ijrmhm.2019.105122.
31. A. Oponowicz, M. Marciszko-Wiąckowska, A. Baczmański, M. Klaus, C. Genzel, S. Wroński, K. Kollbek, M. Wróbel, Gradient of Residual Stress and Lattice Parameter in Mechanically Polished Tungsten Measured Using Classical X-rays and Synchrotron Radiation, Metallurgical and Materials Transactions A 51 (2020) 5945–5957. https://doi.org/10.1007/s11661-020-05967-y.
32. A. Iveković, N. Omidvari, B. Vrancken, K. Lietaert, L. Thijs, K. Vanmeensel, J. Vleugels, J.-P. Kruth, Selective laser melting of tungsten and tungsten alloys, Int J Refract Metals Hard Mater 72 (2018) 27–32. https://doi.org/10.1016/j.ijrmhm.2017.12.005.
33. Y. Jia, S. Chang, X. Du, S. Guo, Corrosion Performance of Commercial Alloys and Refractory Metals in Conditions for Electrorefining of Spent Nuclear Fuels, Crystals (Basel) 13 (2023) 817. https://doi.org/10.3390/cryst13050817.
34. Q. Wei, K.T. Ramesh, B.E. Schuster, L.J. Kecskes, R.J. Dowding, Nanoengineering opens a new era for tungsten as well, JOM 58 (2006) 40–44. https://doi.org/10.1007/s11837-006-0081-1.

35. S.J. Zinkle, L.J. Ott, D.T. Ingersoll, R.J. Ellis, M.L. Grossbeck, Overview of materials technologies for space nuclear power and propulsion, in: AIP Conf Proc, AIP, 2002: pp. 1063–1073. https://doi.org/10.1063/1.1449838.
36. X. Ren, H. Liu, F. Lu, L. Huang, X. Yi, Effects of processing parameters on the densification, microstructure and mechanical properties of pure tungsten fabricated by optimized selective laser melting: From single and multiple scan tracks to bulk parts, Int J Refract Metals Hard Mater 96 (2021) 105490. https://doi.org/10.1016/j.ijrmhm.2021.105490.
37. S. Bai, J. Liu, P. Yang, H. Huang, L.-M. Yang, Femtosecond fiber laser additive manufacturing of tungsten, in: B. Gu, H. Helvajian, A. Piqué (Eds.), 2016: p. 97380U. https://doi.org/10.1117/12.2217551.
38. A. v. Müller, G. Schlick, R. Neu, C. Anstätt, T. Klimkait, J. Lee, B. Pascher, M. Schmitt, C. Seidel, Additive manufacturing of pure tungsten by means of selective laser beam melting with substrate preheating temperatures up to 1000 ◦ C, Nuclear Materials and Energy 19 (2019) 184–188. https://doi.org/10.1016/j.nme.2019.02.034.
39. F. Feng, Y. Lian, J. Wang, J. Song, B. Yan, X. Liu, Mechanical Properties and Thermal Shock Performance of High-Energy-Rate-Forged W-1%TaC Alloy, Crystals (Basel) 12 (2022) 1047. https://doi.org/10.3390/cryst12081047.
40. D.-Z. Wang, K.-L. Li, C.-F. Yu, J. Ma, W. Liu, Z.-J. Shen, Cracking Behavior in Additively Manufactured Pure Tungsten, Acta Metallurgica Sinica (English Letters) 32 (2019) 127–135. https://doi.org/10.1007/s40195-018-0752-2.
41. E. Lassner, W.-D. Schubert, Tungsten, Springer US, Boston, MA, 1999. https://doi.org/10.1007/978-1-4615-4907-9.
42. R. Mitteau, J.M. Missiaen, P. Brustolin, O. Ozer, A. Durocher, C. Ruset, C.P. Lungu, X. Courtois, C. Dominicy, H. Maier, C. Grisolia, G. Piazza, P. Chappuis, Recent developments toward the use of tungsten as armour material in plasma facing components, Fusion Engineering and Design 82 (2007) 1700–1705. https://doi.org/10.1016/j.fusengdes.2007.01.003.
43. B. Vrancken, R.K. Ganeriwala, M.J. Matthews, Analysis of laser-induced microcracking in tungsten under additive manufacturing conditions: Experiment and simulation, Acta Mater 194 (2020) 464–472. https://doi.org/10.1016/j.actamat.2020.04.060.
44. A.H. Elsayed, M.A. Sayed, O.M. Dawood, W.M. Daoush, Effect of Transition Metals Oxides on the Physical and Mechanical Properties of Sintered Tungsten Heavy Alloys, Crystals (Basel) 10 (2020) 825. https://doi.org/10.3390/cryst10090825.
45. L. Wang, J. Wu, D. Zhang, Properties evolution of additive manufacture used tungsten powders prepared by radio frequency induction plasma, Int J Refract Metals Hard Mater 67 (2017) 90–97. https://doi.org/10.1016/j.ijrmhm.2017.05.007.
46. X. Zi, C. Chen, X. Wang, P. Wang, X. Zhang, K. Zhou, Spheroidisation of tungsten powder by radio frequency plasma for selective laser melting, Materials Science and Technology 34 (2018) 735–742. https://doi.org/10.1080/02670836.2017.1410955.
47. D.D. Gu, W. Meiners, K. Wissenbach, R. Poprawe, Laser additive manufacturing of metallic components: materials, processes and mechanisms, International Materials Reviews 57 (2012) 133–164. https://doi.org/10.1179/1743280411Y.0000000014.
48. M. Guo, D. Gu, L. Xi, L. Du, H. Zhang, J. Zhang, Formation of scanning tracks during Selective Laser Melting (SLM) of pure tungsten powder: Morphology, geometric features and forming mechanisms, Int J Refract Metals Hard Mater 79 (2019) 37–46. https://doi.org/10.1016/j.ijrmhm.2018.11.003.
49. S. Wen, C. Wang, Y. Zhou, L. Duan, Q. Wei, S. Yang, Y. Shi, High-density tungsten fabricated by selective laser melting: Densification, microstructure, mechanical and thermal performance, Opt Laser Technol 116 (2019) 128–138. https://doi.org/10.1016/j.optlastec.2019.03.018.
50. O. Gokcekaya, T. Ishimoto, T. Todo, P. Wang, T. Nakano, Influence of powder characteristics on densification via crystallographic texture formation: Pure tungsten prepared by laser powder bed fusion, Additive Manufacturing Letters 1 (2021) 100016. https://doi.org/10.1016/j.addlet.2021.100016.
51. G. Yang, P. Yang, K. Yang, N. Liu, L. Jia, J. Wang, H. Tang, Effect of processing parameters on the density, microstructure and strength of pure tungsten fabricated by selective electron beam melting, Int J Refract Metals Hard Mater 84 (2019) 105040. https://doi.org/10.1016/j.ijrmhm.2019.105040.
52. P.K. Gokuldoss, S. Kolla, J. Eckert, Additive Manufacturing Processes: Selective Laser Melting, Electron Beam Melting and Binder Jetting—Selection Guidelines, Materials 10 (2017) 672. https://doi.org/10.3390/ma10060672.
53. C. Klahn, B. Leutenecker, M. Meboldt, Design Strategies for the Process of Additive Manufacturing, Procedia CIRP 36 (2015) 230–235. https://doi.org/10.1016/j.procir.2015.01.082.
54. B. Vrancken, W.E. King, M.J. Matthews, In-situ characterization of tungsten microcracking in Selective Laser Melting, Procedia CIRP 74 (2018) 107–110. https://doi.org/10.1016/j.procir.2018.08.050.

55. A.T. Sidambe, Y. Tian, P.B. Prangnell, P. Fox, Effect of processing parameters on the densification, microstructure and crystallographic texture during the laser powder bed fusion of pure tungsten, Int J Refract Metals Hard Mater 78 (2019) 254–263. https://doi.org/10.1016/j.ijrmhm.2018.10.004.
56. P. Rebesan, M. Bonesso, C. Gennari, R. Dima, A. Pepato, M. Vedani, Tungsten Fabricated by Laser Powder Bed Fusion, BHM Berg- Und Hüttenmännische Monatshefte 166 (2021) 263–269. https://doi.org/10.1007/s00501-021-01109-y.
57. C. Tan, K. Zhou, W. Ma, B. Attard, P. Zhang, T. Kuang, Selective laser melting of high-performance pure tungsten: parameter design, densification behavior and mechanical properties, Sci Technol Adv Mater 19 (2018) 370–380. https://doi.org/10.1080/14686996.2018.1455154.
58. J. Chen, K. Li, Y. Wang, L. Xing, C. Yu, H. Liu, J. Ma, W. Liu, Z. Shen, The effect of hot isostatic pressing on thermal conductivity of additively manufactured pure tungsten, Int J Refract Metals Hard Mater 87 (2020) 105135. https://doi.org/10.1016/j.ijrmhm.2019.105135.
59. A.C. Field, L.N. Carter, N.J.E. Adkins, M.M. Attallah, M.J. Gorley, M. Strangwood, The Effect of Powder Characteristics on Build Quality of High-Purity Tungsten Produced via Laser Powder Bed Fusion (LPBF), Metallurgical and Materials Transactions A 51 (2020) 1367–1378. https://doi.org/10.1007/s11661-019-05601-6.
60. M. Guo, D. Gu, L. Xi, H. Zhang, J. Zhang, J. Yang, R. Wang, Selective laser melting additive manufacturing of pure tungsten: Role of volumetric energy density on densification, microstructure and mechanical properties, Int J Refract Metals Hard Mater 84 (2019) 105025. https://doi.org/10.1016/j.ijrmhm.2019.105025.
61. Z. Hu, Y. Zhao, K. Guan, Z. Wang, Z. Ma, Pure tungsten and oxide dispersion strengthened tungsten manufactured by selective laser melting: Microstructure and cracking mechanism, Addit Manuf 36 (2020) 101579. https://doi.org/10.1016/j.addma.2020.101579.
62. D. Wang, C. Yu, X. Zhou, J. Ma, W. Liu, Z. Shen, Dense Pure Tungsten Fabricated by Selective Laser Melting, Applied Sciences 7 (2017) 430. https://doi.org/10.3390/app7040430.
63. B. Vrancken, R.K. Ganeriwala, A.A. Martin, M.J. Matthews, Microcrack mitigation during laser scanning of tungsten via preheating and alloying strategies, Addit Manuf 46 (2021) 102158. https://doi.org/10.1016/j.addma.2021.102158.
64. Z. Xiong, P. Zhang, C. Tan, D. Dong, W. Ma, K. Yu, Selective Laser Melting and Remelting of Pure Tungsten, Adv Eng Mater 22 (2020). https://doi.org/10.1002/adem.201901352.
65. X. Zhou, X. Liu, D. Zhang, Z. Shen, W. Liu, Balling phenomena in selective laser melted tungsten, J Mater Process Technol 222 (2015) 33–42. https://doi.org/10.1016/j.jmatprotec.2015.02.032.
66. Y. Wu, Manufacturing of tungsten and tungsten composites for fusion application via different routes, Tungsten 1 (2019) 80–90. https://doi.org/10.1007/s42864-019-00011-y.
67. D. Wang, Z. Wang, K. Li, J. Ma, W. Liu, Z. Shen, Cracking in laser additively manufactured W: Initiation mechanism and a suppression approach by alloying, Mater Des 162 (2019) 384–393. https://doi.org/10.1016/j.matdes.2018.12.010.
68. J. Braun, L. Kaserer, J. Stajkovic, K.-H. Leitz, B. Tabernig, P. Singer, P. Leibenguth, C. Gspan, H. Kestler, G. Leichtfried, Molybdenum and tungsten manufactured by selective laser melting: Analysis of defect structure and solidification mechanisms, Int J Refract Metals Hard Mater 84 (2019) 104999. https://doi.org/10.1016/j.ijrmhm.2019.104999.
69. T. Yamamoto, M. Hara, Y. Hatano, Effects of fabrication conditions on the microstructure, pore characteristics and gas retention of pure tungsten prepared by laser powder bed fusion, Int J Refract Metals Hard Mater 95 (2021) 105410. https://doi.org/10.1016/j.ijrmhm.2020.105410.
70. R.K. Enneti, R. Morgan, S. V. Atre, Effect of process parameters on the Selective Laser Melting (SLM) of tungsten, Int J Refract Metals Hard Mater 71 (2018) 315–319. https://doi.org/10.1016/j.ijrmhm.2017.11.035.
71. D. Zhang, Q. Cai, J. Liu, Formation of Nanocrystalline Tungsten by Selective Laser Melting of Tungsten Powder, Materials and Manufacturing Processes 27 (2012) 1267–1270. https://doi.org/10.1080/10426914.2012.663119.
72. J. Zhang, D. Gu, Y. Yang, H. Zhang, H. Chen, D. Dai, K. Lin, Influence of Particle Size on Laser Absorption and Scanning Track Formation Mechanisms of Pure Tungsten Powder During Selective Laser Melting, Engineering 5 (2019) 736–745. https://doi.org/10.1016/j.eng.2019.07.003.
73. K. Deprez, S. Vandenberghe, K. Van Audenhaege, J. Van Vaerenbergh, R. Van Holen, Rapid additive manufacturing of MR compatible multipinhole collimators with selective laser melting of tungsten powder, Med Phys 40 (2013). https://doi.org/10.1118/1.4769122.
74. A.T. Sidambe, D.S. Judson, S.J. Colosimo, P. Fox, Laser powder bed fusion of a pure tungsten ultra-fine single pinhole collimator for use in gamma ray detector characterisation, Int J Refract Metals Hard Mater 84 (2019) 104998. https://doi.org/10.1016/j.ijrmhm.2019.104998.
75. J.I. Gear, J. Taprogge, O. White, G.D. Flux, Characterisation of the attenuation properties of 3D-printed tungsten for use in gamma camera collimation, EJNMMI Phys 6 (2019) 1. https://doi.org/10.1186/s40658-018-0238-3.

76. K. Zhou, W. Chen, Y. Yang, R. Li, L. Dong, Y.-Q. Fu, Microstructure and mechanical behavior of porous tungsten skeletons synthesized by selected laser melting, Int J Refract Metals Hard Mater 103 (2022) 105769. https://doi.org/10.1016/j.ijrmhm.2021.105769.
77. P. Morcos, A. Elwany, I. Karaman, R. Arróyave, Review: additive manufacturing of pure tungsten and tungsten-based alloys, J Mater Sci 57 (2022) 9769–9806. https://doi.org/10.1007/s10853-022-07183-y.
78. S. Omole, A. Lunt, S. Kirk, A. Shokrani, Advanced Processing and Machining of Tungsten and Its Alloys, Journal of Manufacturing and Materials Processing 6 (2022) 15. https://doi.org/10.3390/jmmp6010015.
79. S.-H. Pan, G.-C. Yao, Y.-N. Cui, F.-S. Meng, C. Luo, T.-Q. Zheng, G. Singh, Additive manufacturing of tungsten, tungsten-based alloys, and tungsten matrix composites, Tungsten 5 (2023) 1–31. https://doi.org/10.1007/s42864-022-00153-6.
80. A. Talignani, R. Seede, A. Whitt, S. Zheng, J. Ye, I. Karaman, M.M. Kirka, Y. Katoh, Y.M. Wang, A review on additive manufacturing of refractory tungsten and tungsten alloys, Addit Manuf 58 (2022) 103009. https://doi.org/10.1016/j.addma.2022.103009.
81. M. Galati, Electron beam melting process, in: Addit Manuf, Elsevier, 2021: pp. 277–301. https://doi.org/10.1016/B978-0-12-818411-0.00014-8.
82. E.A.I. Ellis, M.A. Sprayberry, C. Ledford, J.P. Hankwitz, M.M. Kirka, C.D. Rock, T.J. Horn, Y. Katoh, R.R. Dehoff, Processing of tungsten through electron beam melting, Journal of Nuclear Materials 555 (2021) 153041. https://doi.org/10.1016/j.jnucmat.2021.153041.
83. H. Zhang, P.R. Carriere, E.D. Amoako, C.D. Rock, S.U. Thielk, C.G. Fletcher, T.J. Horn, Microstructure and Elevated Temperature Flexure Testing of Tungsten Produced by Electron Beam Additive Manufacturing, JOM 75 (2023) 4094–4107. https://doi.org/10.1007/s11837-023-06045-5.
84. D. Dorow-Gerspach, A. Kirchner, Th. Loewenhoff, G. Pintsuk, T. Weißgärber, M. Wirtz, Additive manufacturing of high density pure tungsten by electron beam melting, Nuclear Materials and Energy 28 (2021) 101046. https://doi.org/10.1016/j.nme.2021.101046.
85. J. Wang, D. Yao, M. Li, X. An, S. Li, W. Hou, X. Zhang, G. Yang, J. Wang, L. Wang, Hierarchical effects of multi-layer powder spreading in the electron beam powder bed fusion additive manufacturing of pure tungsten material, Addit Manuf 55 (2022) 102835. https://doi.org/10.1016/j.addma.2022.102835.
86. X. Zhao, N. An, G. Yang, J. Wang, H. Tang, M. Li, J. Zhou, Enhancing standard finite element codes with POD for reduced order thermal analysis: Application to electron beam melting of pure tungsten, Mater Today Commun 29 (2021) 102796. https://doi.org/10.1016/j.mtcomm.2021.102796.
87. P. Fernandez-Zelaia, M. Kirka, Q. Campbell, J. Ortega Rojas, A. Marquez Rossy, C. Ledford, Electron Beam Powder Bed Fusion Additive Manufacturing of Refractory Metals, in: United States, 2021. https://www.osti.gov/biblio/1832704.
88. W.-B. Liao, Z.-Y. Liu, M.-J. He, C. Feng, F. Wang, J. Huang, Effect of Electron Beam Remelting Treatments on the Microstructure and Properties of Atmospheric Plasma Sprayed Tungsten Coatings, Journal of Thermal Spray Technology 30 (2021) 2128–2137. https://doi.org/10.1007/s11666-021-01281-0.
89. W. Jeong, Y.-S. Kwon, D. Kim, Three-dimensional printing of tungsten structures by directed energy deposition, Materials and Manufacturing Processes 34 (2019) 986–992. https://doi.org/10.1080/10426914.2019.1594253.
90. G. Marinelli, F. Martina, H. Lewtas, D. Hancock, S. Mehraban, N. Lavery, S. Ganguly, S. Williams, Microstructure and thermal properties of unalloyed tungsten deposited by Wire + Arc Additive Manufacture, Journal of Nuclear Materials 522 (2019) 45–53. https://doi.org/10.1016/j.jnucmat.2019.04.049.
91. Y.P. Wang, S.Y. Ma, X.S. Yang, Y.Z. Zhou, X. Liu, J.F. Li, J.J. Zhang, C. Li, X.Y. Wang, G.M. Le, Y. Zhang, Microstructure and strengthening mechanisms of 90W–7Ni–3Fe alloys prepared using laser melting deposition, J Alloys Compd 838 (2020) 155545. https://doi.org/10.1016/j.jallcom.2020.155545.
92. G.-Y. Wang, S.-N. Gu, S. Yang, Microstructure and properties of tungsten heavy alloys fabricated by laser direct deposition, Materials Science and Technology 33 (2017) 415–420. https://doi.org/10.1080/02670836.2016.1221492.
93. C. Li, S. Ma, X. Liu, J. Li, G. Le, Microstructures and properties of 80W-20Fe alloys prepared using laser melting deposition process, Int J Refract Metals Hard Mater 77 (2018) 113–119. https://doi.org/10.1016/j.ijrmhm.2018.08.005.
94. G. Wang, X. Sun, M. Huang, Y. Qin, Y. Yao, S. Yang, Influence of processing parameters on the microstructure and tensile property of 85 W-15Ni produced by laser direct deposition, Int J Refract Metals Hard Mater 82 (2019) 227–233. https://doi.org/10.1016/j.ijrmhm.2019.04.016.
95. S. Zhou, L. Wang, Y.-J. Liang, Y. Zhu, R. Jian, B. Wang, L. Wang, Y. Xue, F. Wang, H. Cai, Y. Ren, A strategy to achieve high-strength WNiFe composite-like alloys with low W content by laser melting deposition, Mater Des 190 (2020) 108554. https://doi.org/10.1016/j.matdes.2020.108554.
96. T. DebRoy, H.L. Wei, J.S. Zuback, T. Mukherjee, J.W. Elmer, J.O. Milewski, A.M. Beese, A. Wilson-Heid, A. De, W. Zhang, Additive manufacturing of metallic components – Process, structure and properties, Prog Mater Sci 92 (2018) 112–224. https://doi.org/10.1016/j.pmatsci.2017.10.001.

97. C. Li, Y. Wang, S. Ma, X. Yang, J. Li, Y. Zhou, X. Liu, J. Tang, X. Wang, G. Le, Densification, microstructural evolutions of 90W-7Ni-3Fe tungsten heavy alloys during laser melting deposition process, Int J Refract Metals Hard Mater 91 (2020) 105254. https://doi.org/10.1016/j.ijrmhm.2020.105254.
98. M.T. Stawovy, K. Myers, S. Ohm, Binder jet printing of tungsten heavy alloy, Int J Refract Metals Hard Mater 83 (2019) 104981. https://doi.org/10.1016/j.ijrmhm.2019.104981.
99. V.V.K. Doddapaneni, K. Lee, H.E. Aysal, B.K. Paul, S. Pasebani, K.A. Sierros, C.E. Okwudire, C. Chang, A Review on Progress, Challenges, and Prospects of Material Jetting of Copper and Tungsten, Nanomaterials 13 (2023) 2303. https://doi.org/10.3390/nano13162303.
100. M. Ottensmeyer, H. Sabet, L. Furenlid, M. May, M. Kupinski, Collimator fabrication techniques: a comparative study, Journal of Nuclear Medicine 64 (2023) P1600. http://jnm.snmjournals.org/content/64/supplement_1/P1600.abstract.
101. A. Bose, J.P. Reidy, N. Tuncer, L. Jorgensen, Processing of tungsten heavy alloy by extrusion-based additive manufacturing, Int J Refract Metals Hard Mater 110 (2023) 106021. https://doi.org/10.1016/j.ijrmhm.2022.106021.
102. N. Huang, O.J. Cook, A.P. Argüelles, A.M. Beese, Review of Process–Structure–Property Relationships in Metals Fabricated Using Binder Jet Additive Manufacturing, Metallography, Microstructure, and Analysis 12 (2023) 883–905. https://doi.org/10.1007/s13632-023-00998-4.
103. S. Zhou, Y.-J. Liang, Y. Zhu, B. Wang, L. Wang, Y. Xue, Ultrashort-time liquid phase sintering of high-performance fine-grain tungsten heavy alloys by laser additive manufacturing, J Mater Sci Technol 90 (2021) 30–36. https://doi.org/10.1016/j.jmst.2021.02.032.
104. A. Bose, C.A. Schuh, J.C. Tobia, N. Tuncer, N.M. Mykulowycz, A. Preston, A.C. Barbati, B. Kernan, M.A. Gibson, D. Krause, T. Brzezinski, J. Schroers, R. Fulop, J.S. Myerberg, M. Sowerbutts, Y.-M. Chiang, A. John Hart, E.M. Sachs, E.E. Lomeli, A.C. Lund, Traditional and additive manufacturing of a new Tungsten heavy alloy alternative, Int J Refract Metals Hard Mater 73 (2018) 22–28. https://doi.org/10.1016/j.ijrmhm.2018.01.019.
105. Z.-Y. Du, Y.-Q. Lv, Y. Han, J.-L. Fan, L. Ye, Sintering densification behavior and kinetic mechanism of nano-tungsten powder prepared by sol-spray drying, Tungsten 2 (2020) 371–380. https://doi.org/10.1007/s42864-020-00069-z.
106. Y. Han, J. Fan, T. Liu, H. Cheng, J. Tian, The effect of trace nickel additive and ball milling treatment on the near-full densification behavior of ultrafine tungsten powder, Int J Refract Metals Hard Mater 34 (2012) 18–26. https://doi.org/10.1016/j.ijrmhm.2012.02.014.
107. S.M. Thompson, L. Bian, N. Shamsaei, A. Yadollahi, An overview of Direct Laser Deposition for additive manufacturing; Part I: Transport phenomena, modeling and diagnostics, Addit Manuf 8 (2015) 36–62. https://doi.org/10.1016/j.addma.2015.07.001.
108. T. Karafi, A. Tahiri, H. Chabba, M. Idiri, B. Boubeker, Effect of Grain-Size in Nanocrystalline Tungsten on Hardness and Dislocation Density: A Molecular Dynamics Study, Crystals (Basel) 13 (2023) 469. https://doi.org/10.3390/cryst13030469.
109. N. V. Kozyrev, V. V. Gordeev, Thermodynamic Properties and Equation of State for Tungsten, Crystals (Basel) 13 (2023) 1470. https://doi.org/10.3390/cryst13101470.
110. C. Wei, L. Liu, Y. Gu, Y. Huang, Q. Chen, Z. Li, L. Li, Multi-material additive-manufacturing of tungsten - copper alloy bimetallic structure with a stainless-steel interlayer and associated bonding mechanisms, Addit Manuf 50 (2022) 102574. https://doi.org/10.1016/j.addma.2021.102574.
111. V. Griffiths, J.P. Scanlan, M.H. Eres, A. Martinez-Sykora, P. Chinchapatnam, Cost-driven build orientation and bin packing of parts in Selective Laser Melting (SLM), Eur J Oper Res 273 (2019) 334–352. https://doi.org/10.1016/j.ejor.2018.07.053.
112. K. Ren, Y. Di, G. Wang, L. Wang, H. Wang, Y. Rong, Forward calculation model for utilization of energy and mass in laser-directed energy deposition, Addit Manuf 68 (2023) 103512. https://doi.org/10.1016/j.addma.2023.103512.
113. A. Mohammadhosseini, S.H. Masood, D. Fraser, M. Jahedi, Dynamic compressive behaviour of Ti-6Al-4V alloy processed by electron beam melting under high strain rate loading, Adv Manuf 3 (2015) 232–243. https://doi.org/10.1007/s40436-015-0119-0.
114. S.F. Yang, C.W. Li, A.Y. Chen, B. Gan, J.F. Gu, Microstructure and corrosion resistance of stainless steel manufactured by laser melting deposition, J Manuf Process 65 (2021) 418–427. https://doi.org/10.1016/j.jmapro.2021.03.051.
115. M. Ziaee, N.B. Crane, Binder jetting: A review of process, materials, and methods, Addit Manuf 28 (2019) 781–801. https://doi.org/10.1016/j.addma.2019.05.031.
116. T. Mukherjee, T. DebRoy, A digital twin for rapid qualification of 3D printed metallic components, Appl Mater Today 14 (2019) 59–65. https://doi.org/10.1016/j.apmt.2018.11.003.
117. M. Matthews, J. Trapp, G. Guss, A. Rubenchik, Direct measurements of laser absorptivity during metal melt pool formation associated with powder bed fusion additive manufacturing processes, J Laser Appl 30 (2018). https://doi.org/10.2351/1.5040636.

118. R. Enneti, R. Morgan, T. Wolfe, A. Harooni, S. Volk, Direct Metal Laser Sintering (DMLS) of Tungsten Powders, in: Proceedings for Additive Manufacturing with Powder Metallurgy, 2017.
119. J. Li, Z. Wei, B. Zhou, Y. Wu, S.-G. Chen, Z. Sun, Densification, Microstructure and Properties of 90W-7Ni-3Fe Fabricated by Selective Laser Melting, Metals (Basel) 9 (2019) 884. https://doi.org/10.3390/met9080884.
120. Y. Xia, Z. Dong, X. Guo, Q. Tian, Y. Liu, Towards a circular metal additive manufacturing through recycling of materials: A mini review, J Cent South Univ 27 (2020) 1134–1145. https://doi.org/10.1007/s11771-020-4354-6.
121. P. Gradl, O.R. Mireles, N. Andrews, Introduction to Additive Manufacturing for Propulsion and Energy Systems, in: Propulsion Energy and Forum 2021, 2021.
122. A. Sidambe, P. Fox, Analysis of melt pool during the laser powder bed fusion of tungsten, in: RAPDASA 2019 Conference and Exhibition, 2019.
123. L.M. Sochalski-Kolbus, E.A. Payzant, P.A. Cornwell, T.R. Watkins, S.S. Babu, R.R. Dehoff, M. Lorenz, O. Ovchinnikova, C. Duty, Comparison of Residual Stresses in Inconel 718 Simple Parts Made by Electron Beam Melting and Direct Laser Metal Sintering, Metallurgical and Materials Transactions A 46 (2015) 1419–1432. https://doi.org/10.1007/s11661-014-2722-2.
124. J. Xue, Z. Feng, J. Tang, C. Tang, Z. Zhao, Selective laser melting additive manufacturing of tungsten with niobium alloying: Microstructure and suppression mechanism of microcracks, J Alloys Compd 874 (2021) 159879. https://doi.org/10.1016/j.jallcom.2021.159879.
125. G.K.L. Ng, A.E.W. Jarfors, G. Bi, H.Y. Zheng, Porosity formation and gas bubble retention in laser metal deposition, Applied Physics A 97 (2009) 641–649. https://doi.org/10.1007/s00339-009-5266-3.
126. M. Zhong, W. Liu, G. Ning, L. Yang, Y. Chen, Laser direct manufacturing of tungsten nickel collimation component, J Mater Process Technol 147 (2004) 167–173. https://doi.org/10.1016/j.jmatprotec.2003.12.009.
127. J. Huang, M. Li, J. Wang, Z. Pei, P. Mclntyre, C. Ma, Selective laser melting of tungsten: Effects of hatch distance and point distance on pore formation, J Manuf Process 61 (2021) 296–302. https://doi.org/10.1016/j.jmapro.2020.11.034.
128. J. Li, Y. Wu, B. Zhou, Z. Wei, Laser Powder Bed Fusion of Pure Tungsten: Effects of Process Parameters on Morphology, Densification, Microstructure, Materials 14 (2020) 165. https://doi.org/10.3390/ma14010165.
129. J. Dong, S. Liu, H. Chen, D. Li, T. Zhang, C. Chen, K. Zhou, Effect of atmosphere on the microstructure and properties of additively manufactured tungsten, Materials Science and Technology 36 (2020) 1988–1996. https://doi.org/10.1080/02670836.2020.1852680.
130. A.W. Adamson, Potential distortion model for contact angle and spreading. II. Temperature dependent effects, J Colloid Interface Sci 44 (1973) 273–281. https://doi.org/10.1016/0021-9797(73)90219-1.
131. Y. Muramatsu, K. Halada, T. Dan, Y. Isoda, Solid-Liquid Interfacial Tension of the W-Cu System, Journal of the Japan Institute of Metals 54 (1990) 679–684. https://doi.org/10.2320/jinstmet1952.54.6_679.
132. S. Pan, Z. Guan, G. Yao, J. Yuan, X. Li, Mo-enhanced chemical stability of TiC nanoparticles in molten Al, J Alloys Compd 856 (2021) 158169. https://doi.org/10.1016/j.jallcom.2020.158169.
133. C. Wei, H. Gu, Y. Gu, L. Liu, Y. Huang, D. Cheng, Z. Li, L. Li, Abnormal interfacial bonding mechanisms of multi-material additive-manufactured tungsten–stainless steel sandwich structure, International Journal of Extreme Manufacturing 4 (2022) 025002. https://doi.org/10.1088/2631-7990/ac5f10.
134. K. Li, D. Wang, L. Xing, Y. Wang, C. Yu, J. Chen, T. Zhang, J. Ma, W. Liu, Z. Shen, Crack suppression in additively manufactured tungsten by introducing secondary-phase nanoparticles into the matrix, Int J Refract Metals Hard Mater 79 (2019) 158–163. https://doi.org/10.1016/j.ijrmhm.2018.11.013.
135. H. Kurishita, S. Matsuo, H. Arakawa, T. Sakamoto, S. Kobayashi, K. Nakai, H. Okano, H. Watanabe, N. Yoshida, Y. Torikai, Y. Hatano, T. Takida, M. Kato, A. Ikegaya, Y. Ueda, M. Hatakeyama, T. Shikama, Current status of nanostructured tungsten-based materials development, Phys Scr T159 (2014) 014032. https://doi.org/10.1088/0031-8949/2014/T159/014032.
136. D. Nagy, S.A. Humphry-Baker, An oxidation mechanism map for tungsten, Scr Mater 209 (2022) 114373. https://doi.org/10.1016/j.scriptamat.2021.114373.
137. A. Warren, A. Nylund, I. Olefjord, Oxidation of tungsten and tungsten carbide in dry and humid atmospheres, Int J Refract Metals Hard Mater 14 (1996) 345–353. https://doi.org/10.1016/S0263-4368(96)00027-3.
138. E.M. Savitskii, G.S. Burkhanov, Physical Metallurgy of Refractory Metals and Alloys, Springer US, Boston, MA, 1995. https://doi.org/10.1007/978-1-4684-1572-8.
139. C.C. Eckley, R.A. Kemnitz, C.P. Fassio, C.R. Hartsfield, T.A. Leonhardt, Selective Laser Melting of Tungsten-Rhenium Alloys, JOM 73 (2021) 3439–3450. https://doi.org/10.1007/s11837-021-04776-x.
140. T. Yamamoto, M. Hara, Y. Hatano, Cracking behavior and microstructural, mechanical and thermal characteristics of tungsten–rhenium binary alloys fabricated by laser powder bed fusion, Int J Refract Metals Hard Mater 100 (2021) 105651. https://doi.org/10.1016/j.ijrmhm.2021.105651.
141. W. Klopp, W. Witzke, P. Raffo, Mechanical properties of dilute tungsten-rhenium alloys, 1966.

142. D.Q. Zhang, Z.H. Liu, Q.Z. Cai, J.H. Liu, C.K. Chua, Influence of Ni content on microstructure of W–Ni alloy produced by selective laser melting, Int J Refract Metals Hard Mater 45 (2014) 15–22. https://doi.org/10.1016/j.ijrmhm.2014.02.007.
143. D. Zhang, Q. Cai, J. Liu, R. Li, Research on Process and Microstructure Formation of W-Ni-Fe Alloy Fabricated by Selective Laser Melting, J Mater Eng Perform 20 (2011) 1049–1054. https://doi.org/10.1007/s11665-010-9720-3.
144. A. Iveković, M.L. Montero-Sistiaga, K. Vanmeensel, J.-P. Kruth, J. Vleugels, Effect of processing parameters on microstructure and properties of tungsten heavy alloys fabricated by SLM, Int J Refract Metals Hard Mater 82 (2019) 23–30. https://doi.org/10.1016/j.ijrmhm.2019.03.020.
145. Z. Hu, Y. Liu, J. Wu, J. Dong, Z. Ma, Y. Liu, The simultaneous improvement of strength and ductility of the 93W-4.6Ni-2.4Fe prepared by additive manufacturing via optimizing sintering post-treatment, Addit Manuf 46 (2021) 102216. https://doi.org/10.1016/j.addma.2021.102216.
146. H. Chen, X. Zi, Y. Han, J. Dong, S. Liu, C. Chen, Microstructure and mechanical properties of additive manufactured W-Ni-Fe-Co composite produced by selective laser melting, Int J Refract Metals Hard Mater 86 (2020) 105111. https://doi.org/10.1016/j.ijrmhm.2019.105111.
147. M. Wang, R. Li, T. Yuan, C. Chen, M. Zhang, Q. Weng, J. Yuan, Selective laser melting of W-Ni-Cu composite powder: Densification, microstructure evolution and nano-crystalline formation, Int J Refract Metals Hard Mater 70 (2018) 9–18. https://doi.org/10.1016/j.ijrmhm.2017.09.004.
148. A. Yan, Z. Wang, T. Yang, Y. Wang, Z. Ma, Microstructure, thermal physical property and surface morphology of W-Cu composite fabricated via selective laser melting, Mater Des 109 (2016) 79–87. https://doi.org/10.1016/j.matdes.2016.07.049.
149. R. Li, Y. Shi, J. Liu, Z. Xie, Z. Wang, Selective laser melting W–10 wt.% Cu composite powders, The International Journal of Advanced Manufacturing Technology 48 (2010) 597–605. https://doi.org/10.1007/s00170-009-2304-4.
150. G. Wang, Y. Qin, S. Yang, Characterization of laser-powder interaction and particle transport phenomena during laser direct deposition of W–Cu composite, Addit Manuf 37 (2021) 101722. https://doi.org/10.1016/j.addma.2020.101722.
151. Z. Zhou, Z. Tan, D. He, Z. Zhou, L. Cui, Y. Wang, W. Shao, G. Wang, Fabrication of three-dimensional connected W-Cu10Sn composites by selective laser melting, Mater Lett 264 (2020) 127377. https://doi.org/10.1016/j.matlet.2020.127377.
152. K. Li, Y. Li, W. Chen, C. Zhao, Y. Yuan, L. Cheng, T.W. Morgan, W. Liu, Z. Shen, Effect of Ta addition on the fuzz formation of additively manufactured W-based materials, Nuclear Fusion 60 (2020) 064004. https://doi.org/10.1088/1741-4326/ab8a69.
153. K. Li, G. Ma, L. Xing, Y. Wang, C. Yu, J. Chen, J. Ma, G. Wu, W. Liu, Z. Shen, X. Huang, Crack suppression via in-situ oxidation in additively manufactured W-Ta alloy, Mater Lett 263 (2020) 127212. https://doi.org/10.1016/j.matlet.2019.127212.
154. Z. Guo, L. Wang, X.-Z. Wang, Additive manufacturing of W-12Ta(wt%) alloy: Processing and resulting mechanical properties, J Alloys Compd 868 (2021) 159193. https://doi.org/10.1016/j.jallcom.2021.159193.
155. J. Li, Z. Wei, B. Zhou, Y. Wu, S.-G. Chen, Z. Sun, Preparation, microstructure, and microhardness of selective laser-melted W–3Ta sample, J Mater Res 35 (2020) 2016–2024. https://doi.org/10.1557/jmr.2020.71.
156. B. Xiao, W. Jia, H. Tang, J. Wang, L. Zhou, Microstructure and mechanical properties of a newly developed WTaRe refractory alloy by selective electron beam melting, Addit Manuf 54 (2022) 102738. https://doi.org/10.1016/j.addma.2022.102738.
157. B. Xiao, W. Jia, J. Wang, L. Zhou, High-temperature mechanical behaviors of a WTaRe refractory alloy manufactured by selective electron beam melting, Int J Refract Metals Hard Mater 116 (2023) 106371. https://doi.org/10.1016/j.ijrmhm.2023.106371.
158. H. Chen, L. Ye, Y. Han, C. Chen, J. Fan, Additive manufacturing of W–Fe composites using laser metal deposition: Microstructure, phase transformation, and mechanical properties, Materials Science and Engineering: A 811 (2021) 141036. https://doi.org/10.1016/j.msea.2021.141036.
159. Z. Tan, Z. Zhou, X. Wu, Y. Wang, W. Shao, X. Guo, Z. Zhou, Y. Yang, G. Wang, D. He, In situ synthesis of spherical W Mo alloy powder for additive manufacturing by spray granulation combined with thermal plasma spheroidization, Int J Refract Metals Hard Mater 95 (2021) 105460. https://doi.org/10.1016/j.ijrmhm.2020.105460.
160. S. Lang, N. Sun, J. Cao, W. Yu, Z. Yang, S. Hou, Fabrication of Ultra-Fine-Grained W-TiC Alloys by a Simple Ball-Milling and Hydrogen Reduction Method, Materials 14 (2021) 5865. https://doi.org/10.3390/ma14195865.
161. D. Gu, D. Dai, W. Chen, H. Chen, Selective Laser Melting Additive Manufacturing of Hard-to-Process Tungsten-Based Alloy Parts With Novel Crystalline Growth Morphology and Enhanced Performance, J Manuf Sci Eng 138 (2016). https://doi.org/10.1115/1.4032192.

 doi:10.20944/preprints202406.1108.v1

162. J. Chen, C. Zhao, K. Li, M. Li, S. Sun, S. Zhang, J. Ma, W. Liu, Effect of TaC addition on microstructure and microhardness of additively manufactured tungsten, J Alloys Compd 897 (2022) 162978. https://doi.org/10.1016/j.jallcom.2021.162978.
163. N.C. Cole, R.G. Gilliland, G.M. Slaughter, Weldability of tungsten and its alloys, in: American Welding Society 49th Annual Meeting, 1968.
164. A. Bose, R.M. German, Microstructural refinement of W-Ni-Fe heavy alloys by alloying additions, Metallurgical Transactions A 19 (1988) 3100–3103. https://doi.org/10.1007/BF02647738.
165. A. Luo, D.L. Jacobson, K.S. Shin, Solution softening mechanism of iridium and rhenium in tungsten at room temperature, Int J Refract Metals Hard Mater 10 (1991) 107–114. https://doi.org/10.1016/0263-4368(91)90028-M.
166. Y.K. Wang, Z.M. Xie, M.M. Wang, H.W. Deng, J.F. Yang, Y. Jiang, T. Zhang, X.P. Wang, Q.F. Fang, C.S. Liu, The superior thermal stability and tensile properties of hot rolled W-HfC alloys, Int J Refract Metals Hard Mater 81 (2019) 42–48. https://doi.org/10.1016/j.ijrmhm.2019.02.018.
167. T. Leonhardt, Properties of tungsten-rhenium and tungsten-rhenium with hafnium carbide, JOM 61 (2009) 68–71. https://doi.org/10.1007/s11837-009-0107-6.
168. C. Ren, Z.Z. Fang, M. Koopman, B. Butler, J. Paramore, S. Middlemas, Methods for improving ductility of tungsten - A review, Int J Refract Metals Hard Mater 75 (2018) 170–183. https://doi.org/10.1016/j.ijrmhm.2018.04.012.
169. A. Calvo, K. Schlueter, E. Tejado, G. Pintsuk, N. Ordás, I. Iturriza, R. Neu, J.Y. Pastor, C. García-Rosales, Self-passivating tungsten alloys of the system W-Cr-Y for high temperature applications, Int J Refract Metals Hard Mater 73 (2018) 29–37. https://doi.org/10.1016/j.ijrmhm.2018.01.018.